Delft University of Technology
Faculty of Applied Sciences
Department of Radiation, Radionuclides and Reactors

Analysis of Two-Phase Flow Instabilities in Multi-Channel Natural Circulation Systems

Coen Degen

Supervisor: Martin Rohde

Delft, February 2009

Abstract

It is well known that natural circulation Boiling Water Reactors are subject to system-wide density wave instabilities. During the startup of such a reactor, at low pressure and low power conditions, flashing and geysering-induced instabilities may occur due to the strong dependence of the saturation temperature on the local pressure. Previous research showed that these instabilities depend on the applied power, the inlet temperature, the friction distribution and the number of parallel channels.

In order to further study the influence of the number of parallel channels, the current experimental setup CIRCUS at Delft University of Technology is extended to four parallel channels. Comparison with experimental results from the previous single channel and double channel setups, is subsequently used to draw conclusions about channel division. For four parallel channels, six different stability regimes are encountered. It was found that the instabilities in each regime could be explained using three phenomena: flashing, geysering and reverse flow. A clear distinction is shown to exist between in-phase oscillations, which are caused by flashing, geysering and reverse flow phenomena and out-of-phase oscillations, which are exclusively associated with geysering and reverse flow.

Since the ESBWR design will contain many parallel channels, predictions are made for the stability behavior in a setup with n parallel channels. This is accomplished by combining the experimental results with simulations for the in-phase and out-of-phase stability boundaries, based on steady state conditions. The measured transitions between the stability regimes are found to correspond well with the simulations. From this result, a theoretical extrapolation to n channels could be created and it can be concluded that dividing a single channel into n parallel channels will increase the stability of systems at the same operational point in the $N_{pch} - N_{sub}$ plane.

Additionally, the stability of multi-channel systems at uneven power distribution is experimentally investigated using the CIRCUS setup. It is found that in these situations the stability of the system is governed by the channel to which the highest power is applied. Furthermore, the application of a local inlet friction to one of the channels is shown to have a stabilizing effect for systems at the same operational point in the $N_{pch} - N_{sub}$ plane. As a result, it is expected that a combined power and friction skew can be utilized to equalize the heat transferred per unit mass over all channels in multi-channel natural circulation systems.

To ...

Contents

Chapter 1

Introduction

1.1 The need for sustainable nuclear power

The world is running into an energy crisis. We are witnessing a time that combines record breaking human development with a record breaking increase in demand for energy. The great challenge of the 21st century will therefore be making sure that this energy demand can be met, while at the same time dealing with climate change and other environmental hazards. Virtually everyone agrees that fossil fuels will not be the way of the future anymore. Although research into promising and viable alternatives is currently at full speed, it will still take some time before they will contribute significantly to the energy mix.

In the meantime, fossil fuel prices have become volatile and the amount of international quarrels about the delivery of these fuels seems to increase. When a part of Europe was cut off from the supply of natural gas due to a recent conflict between the Ukraine and Russia over its price, Slovakia decided to reemploy two nuclear reactors that were in fact closed as a condition for entering the European Union. Apart from the question if this is a development we should welcome, it exemplifies how most European countries would deal with a sudden energy shortage: they turn to proven technology that is not based on importing large amounts of resources from countries that do not range among their best allies. Since no large scale alternative will be available on short term, nuclear energy becomes an attractive option. At least part of the recent positive shift in political attitude towards nuclear power can be attributed to this fact.

In addition to this, we must not forget that nuclear power has had a significant presence in Europe over the last decades. Some countries more than others, but almost 35% of all European electrical power is produced by nuclear fission even today. It is therefore very unlikely that nuclear power will disappear from our energy mix in the foreseeable future. But of course there is also general concern about the safety of these reactors. Several events in the past have raised both awareness and fear for their application. Although a lot of research into reactor improvements, innovative reactor designs and safety measures has already been conducted, new and improved reactor designs are currently in development that boast even higher standards of safety, while also improving the economics and

sustainability of the nuclear cycle. In short: There is a need for new, more sustainable nuclear power.

This thesis focuses on the stability of the thermal hydraulic system in a reactor of the newest generation currently on the market: The Economic Simplified Boiling Water Reactor (ESBWR). A design by General Electric.

1.2 The ESBWR principle

One of the traditional designs for nuclear reactors is the Boiling Water Reactor (BWR). In these types of reactors, ordinary water is used as a coolant to remove the heat produced by fission processes in the core. The coolant is usually pumped into the core from the bottom and, while rising through the fuel assemblies, slowly starts to boil. At the top of the core, the steam is separated from the liquid coolant and is used to drive one or more turbines that produce electricity by means of a generator. Afterwards the condensed steam is fed back into the system via the periphery of the vessel, also called the downcomer section. A schematic of a typical BWR vessel is shown in figure 1.1a.

Due to the immense power generated within the BWR vessel, a large density difference is created between the coolant in the reactor core and the coolant in the downcomer. This means that the water in the downward channel is heavier than the hot water and steam in the core and as a result a gravity driven current will start to flow through the reactor. This effect is called natural circulation and it is large enough to drive part of the flow through the core. However, natural circulation is not enough to extract all the heat produced during fission from the reactor core. Circulation pumps are necessary to drive the flow of coolant through the core at high power levels. In the most recent BWR design currently in operation, the ABWR (shown in figure 1.1b), these circulation pumps have been placed inside the reactor vessel itself, which is a great increase to safety, but they are still necessary to drive the coolant through the core at high power.

The continuing quest for reactor safety has introduced the need for passively safe systems. This means that the safety of the reactor does not depend on active systems, like pumps, but is governed by natural processes. Making full advantage of the natural circulation effect, a new BWR design was made that achieves this goal: the Economic Simplified BWR (ESBWR), in which the need for circulation pumps was eliminated. To achieve a higher natural circulation level, a taller chimney was installed on top of the core (nearly 28 m), thus increasing the gravitational pressure head. As a result, all heat can be removed from the core by natural circulation during operation of the reactor, which is expected to be about 4500 MWth. A rendering of the ESBWR reactor vessel can be found in figure 1.1c.

Unfortunately, the elimination of the pumps also comes at a cost. At certain operational conditions, especially during the startup of the reactor, thermal hydraulic instabilities may occur due to the feedback between steam production in the chimney and the gravitational driving force of the system. These instabilities give rise to flow oscillations and are undesirable, since they complicate the operation of the reactor and may have a negative effect on the lifespan of the reactor.

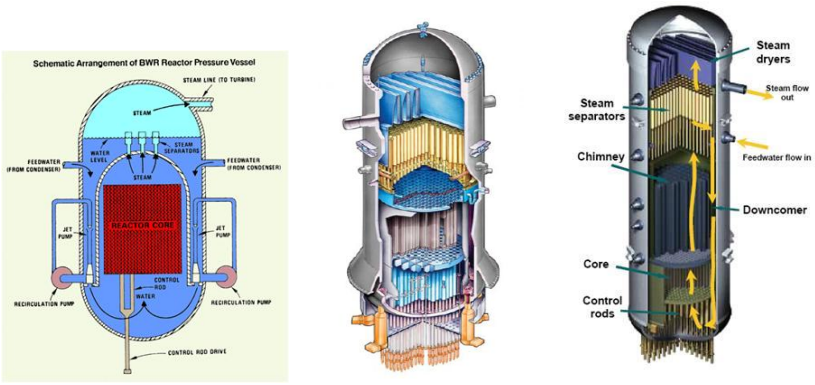

(a) (b) 1.1b (c)

Figure 1.1: Schematics of Boiling Water Reactor vessels of different generations. A typical BWR vessel (a) and the ABWR (b) and the ESBWR (c) reactor vessels.

1.3 Stability of natural circulation Boiling Water Reactors

The ESBWR design does not come with an external pressurization system, but makes use of the vapor created in the core to increase the pressure in the system to approximately 70 bar for nominal operation. Therefore, at the startup of the reactor, this vapor has to be produced first by operating the reactor at low power and (still) low pressure conditions.

This has important implications on the physical properties of the coolant. During nominal, high-pressure operation of the ESBWR, the saturation temperature is practically constant in the chimney section of the facility. At low pressure, however, the saturation temperature is one of the fluid properties that become highly dependent on the pressure level, as can be seen in figure 1.2a. In addition, the moment vapor *is* produced in the system, it will immediately take up a large volume in the chimney, caused by the extremely sharp increase of the void fraction with the flow quality under low pressure conditions, as can be seen in figure 1.2b. As a result of the decreased density in the core, the driving head is significantly enhanced, causing the flow through the system to increase temporarily. Due to the higher flow level, the core is flooded with relatively colder coolant from the downcomer, expelling the vapor and consequently decreasing the density difference again. The resulting oscillations in the flow through the system are commonly referred to as gravity driven density wave oscillations.

Vapor can be produced in the core in different ways. In figure 1.3, this is shown schematically in a static situation at different pressure conditions. In the first figure (a), the reactor is operating a nominal pressure. The saturation temperature, T_{sat}, does not vary significantly over the height of the system. The coolant is heated in the core until it reaches the saturation temperature and vapor is produced. In the low pressure situations of figures 1.3 (b) and (c), however, we see that the saturation temperature varies over the height of the

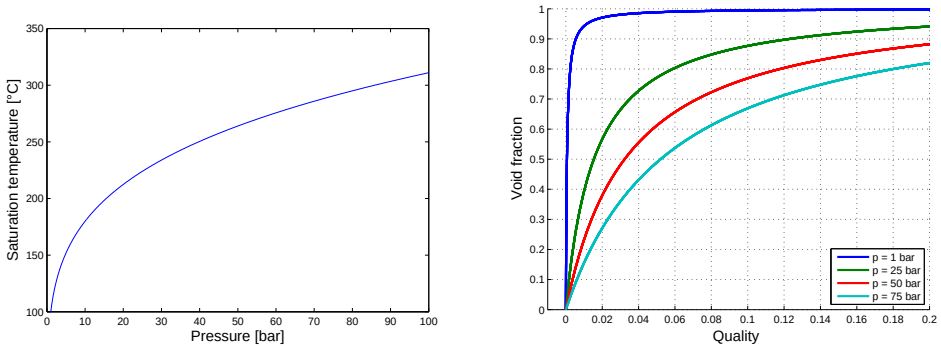

(a) (b)

Figure 1.2: The saturation temperature as a function of the pressure (a) and the void fraction as a function of the flow quality for different system pressures (b).

system due to the decrease in hydrostatic pressure.

At high power and low pressure, the coolant is heated to the saturation temperature in the core. Vapor is consequently produced in the core. The resulting density wave oscillations caused by this effect, will be called geysering throughout the rest of this thesis, as in dynamical conditions they are similar to the well known vapor explosions and subsequent flow reversal. However, during startup of the ESBWR, the power is usually also relatively low, due to the fact that heat transfer to the bulk of the coolant is relatively low as a result of the extensive vapor production. This means that another interesting, but unwanted flow oscillation effect can occur. In figure 1.3 (c) we see that due to the low power, the coolant cannot be heated to the saturation temperature in the core. Nevertheless, the steam production will continue in the unheated chimney section due to the fact that the saturation temperature decreases near the top of the core. At a certain height in the chimney, the temperature of the heated coolant will be equal to the local saturation temperature and vapor will be produced. This effect is referred to as 'void flashing' (or just 'flashing'). In dynamic conditions, this effect causes a oscillations in the mass flow, as explained above.

1.4 Objective

Flashing-induced instabilities have been studied both experimentally and numerically since their existence was first pointed out in the 1950s [2]. The effect has been recreated in several experimental facilities and during an experimental campaign in the Dutch natural circulation BWR Dodewaard [3].

At the department of Physics of Nuclear Reactors at Delft University of Technology, recent experimental and numerical investigations of flashing-induced instabilities have been conducted by Van Bragt [1], Manera [4] and Marcel [5]. Since, evidently, an actual ESBWR-sized experimental facility would be

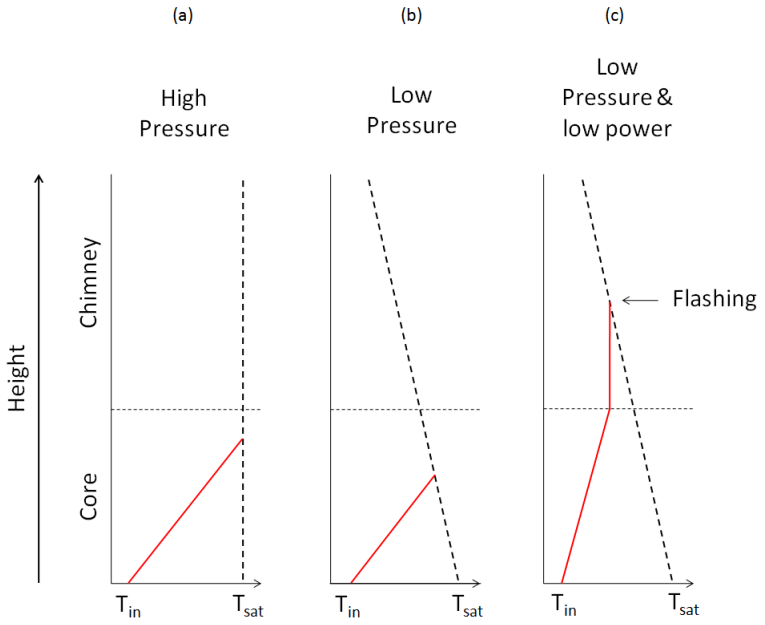

Figure 1.3: Temperature profiles in the reactor vessel at diffent conditions. The dashed line indicated the saturation temperature as a function of height.

very costly and impractical, the scaled facility CIRCUS (CIRCUlation during Startup) was constructed at Delft University of Technology to investigate the stability behavior of the ESBWR at low pressure conditions. It was found that at low pressure and low power conditions, flashing is indeed the main cause of instabilities. It was also shown that an unstable operational region exists between stable single-phase and two-phase operation.

Although much research into the stability of the ESBWR has been conducted, this thesis is concerned with some of the last remaining questions related to its stability at low pressure conditions. It was recommended by Manera [4] that research be conducted into the stability effects of a partitioned chimney. If we take another look at the ESBWR vessel in figure 1.1c, it can be noticed that the chimney section above the core is divided into many separate channels. These channels are installed to guide the two-phase flow in the reactor upwards and to avoid cross flow between neighbouring fuel assemblies, making the behavior in the reactor more predictable and therefore more controllable. Little is known about the stability effects of such a division in a natural circulation system. Some previous experimental work on this subject was conducted by Marcel [5], after fitting the CIRCUS facility with a double channel. Due to the coupling of the channels at the top and the bottom of the facility, several new instability states were found to be introduced. It remained unclear, however, how this division influenced the stability of the reactor as a whole.

The main aim of this thesis is therefore to investigate the effect of dividing the system into many different channels. This investigation can be divided into four key parts:

1. The phenomenology of the four-parallel channel system is studied in detail by analyzing flow characteristics, temperature profiles and vapor production in the system. This will allow description of the different instability regimes in the system and provides insight into the driving phenomena associated with the instabilities. The resulting experimental data will be compared to experiments obtained with the previous single-channel and two parallel-channel setups to make predictions about the behavior of n parallel channel systems.

2. The observed differences between the stability phenomena are used to formulate boundary conditions for a simple steady state model describing the stability boundaries of the parallel channel system. This model will be tested against the available experimental data from the different CIRCUS setups.

3. Consequently, this model is extrapolated to a system with n parallel channels to predict the occurrence of stability regimes in systems that are divided into a larger number of parallel channels.

4. A last objective that was set, is to investigate the effect of a power skew between parallel channels. For this purpose, experiments are conducted in the four parallel channel system, in which the power is varied between channels. Additionally, investigations are conducted into the effect on stability of a proposed method to compensate for a power skew by applying different localized frictional pressure drops over the channels.

1.5 Outline of this thesis

There is hardly any engineering project to be found that can afford not to be concerned about its societal context. Delft University of Technology has decided to emphasize this context by incorporating it into the programme by means of specialized courses on ethics and sustainability. This project was conducted in the framework of the special track Sustainability in Technology and in this light, its place in the societal context is first described in chapter 2.

After that, the CIRCUS facility is briefly described for reference in chapter 3, before continuing to the detailed description and explanation of the diverse instability states found to occur in the system in chapter 4. In this chapter, a connection will also be made with the findings of Manera and Marcel at respectively the single channel- and double channel setup.

In the subsequent chapter 5, a simple steady state model, based on the observations in chapter 4 will be presented. The model is compared to the experimental results by Manera and Marcel and is then extended to a system which is divided into many channels.

Chapter 6 will deal with investigations into the stability behavior of the system under a power skew and the application of localized friction at the bottom of the channels. The implications of the results to the ESBWR will also be discussed in this chapter.

Chapter 2

Sustainability

The issue of sustainability is often a many-sided one. This is definitely the case in relation to nuclear power generation, due to strong (and differing) sentiments that people have regarding its application. Nevertheless, in recent years, the general public seems to have renewed its interest in nuclear power. It is hard to guess if this change in attitude is due to the fact that technology as a whole becomes an ever larger and more accepted part of our daily lives, or perhaps due to the simple fact that nuclear power for once finds itself on the popular side of a waste issue: the discussion about climate change.

This chapter will not be a complete overview of the sustainability of nuclear power. The subject is simply too broad and sometimes too complicated to provide a full account of all the details. Though most of them are interesting and many-sided, this thesis is not the place to discuss them all extensively. Instead, the chapter will focus on the position of nuclear power in the light of modern trends, in particular two themes specifically related to the improvements by the ESBWR: safety and economy.

2.1 Energy crisis

There hardly has been a time in which the discussion about energy has been as global as today. Although worries about peak oil largely seem to have been replaced by outcries on the reduction of CO_2 emissions, the fact remains that the fossil fuel supply is limited. Often even more so in availability, as recent surges in oil prices and conflicts about the delivery of natural gas have shown. Important pockets of fossil fuel reserves are concentrated in only a few countries, that consequently have a large influence on their distribution.

Moreover, in the last decades, we are experiencing unprecedented levels of human development. The incorporation of technology in virtually any part of daily life in the western world and the rapid development of, for example, several Asian countries, have increased the demand for energy even more: Trends that are not expected to weaken over the next decades. In addition, the world's population is still growing rapidly, as can be seen in figure 2.1a, contributing to an estimated 50% rise in energy demand until 2030 [7, 10].

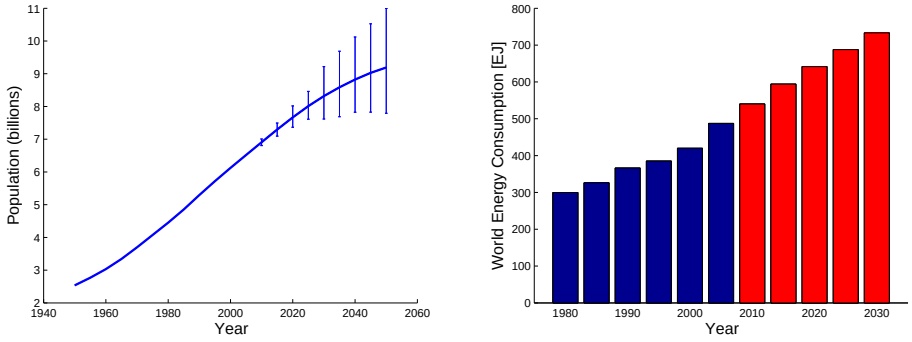

(a) (b)

Figure 2.1: The historic and projected development of the world's population (a) and the total and projected world total energy consumption (b). Sources: UN department of economic and social affairs [9], EIA [10].

Despite remarkable progress in renewable methods of energy supply, e.g. solar, wind and biomass, a secure power supply based on their application is not expected on the short-term. Even the most optimistic scenarios predict no more than a 15% share of these renewables in 2030 [8] Extending the current exponential growth to the year 2050, still only means a renewable share of 45% in the energy mix. It is questionable, however, if the current growth can be sustained at the same pace for all renewables. At the same time, as we will see in the next section, ambitious goals have been set for the reduction of greenhouse gases to the environment. Making sure that there will be enough energy in the long run, without drastically influencing our environment, will therefore be one of the major challenges of the century.

2.2 Climate change

In addition to the rising energy demand, research has shown that it is extremely likely that the warming of the planet is induced by human activity [11]. Through the emission of greenhouse gases, of which especially carbon dioxide plays a significant role, human development is influencing the world's climate. Realization of the extent of the problem has urged governments worldwide to take measures to mitigate the rate of increase of CO_2 in the atmosphere. It is, however, safe to say that limiting these emissions is easier said than done under the trends described in the last section.

The Carbon Mitigation Initiative from the Princeton Environmental Institute [12] has an insightful way of demonstrating the seriousness of the problem. In figure 2.2a, the historical CO_2 emissions have been plotted. In the same figure, predictions of future emission levels are displayed, based on a "business as usual" scenario. To be able to halt the increase of CO_2 emissions in the future, measures should be taken that amount to a total reduction of 8 billion Tons of CO_2 yearly in 2055. If we divide this amount (the stabilization triangle

in figure 2.2a) into eight equal 'wedges,' we can suggest eight measures that would save up to 1 GTon of emissions in 2055. This is depicted schematically in figure 2.2b.

In the list below, several measures proposed by the CMI [12] that would amount to such a reduction have been summed up.

- Double the fuel efficiency of the world's cars **or** halve the total distance traveled by car in the world. There are about 600 million cars in the world today, with 2 billion predicted for 2055.
- Produce today's electricity with double the efficiency. Average coal plant efficiency is around 32% nowadays.
- Use today's best efficiency practices in all residential and commercial buildings.
- Build 1000 of today's Carbon storage facilities. There are currently three storage projects that each inject 1 million tons of CO_2 into the ground per year.
- Install 1 million 2 MW windmills to replace coal based electricity. This means increasing the currently installed wind electricity capacity by a factor thirty.
- Install 20.000 square kilometers of solar electricity. This would mean increasing current capacity 700 times.
- Eliminate tropical deforestation **or** plant new forests over an area the size of the continental US.
- Triple the world's nuclear electricity capacity by 2055. The CO_2 emissions in the fuel- and lifecycle of a nuclear power plant are negligible compared to many other means of electricity generation, as can be seen in figure 2.3.

For most of the above measures, it is very questionable if they can be achieved before 2055. Moreover, we would need to achieve *all* of the examples above (or equivalent measures) to only stabilize the total emission of CO_2 in the future. To reduce these levels, we would even have to go through much greater lengths. From this analysis we can conclude that if we are to realistically reduce CO_2 emissions, we must work on it in all possible fields. Due to its low CO_2 emissions and proven availability, nuclear power generation therefore becomes an attractive option and is likely to be part of any solution.

2.3 Nuclear energy today

The use of nuclear energy for commercial power generation has been a topic of vivid discussion in many countries. There have been large differences in governmental policies over the last decades. France, for example, presently derives more than 75% of its electricity from nuclear energy, while the German government (at 25% currently also a major user of nuclear power) has recently

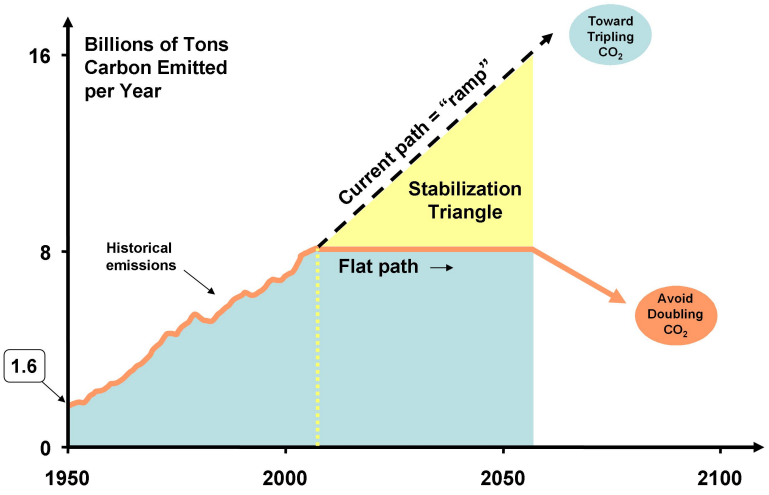

(a)

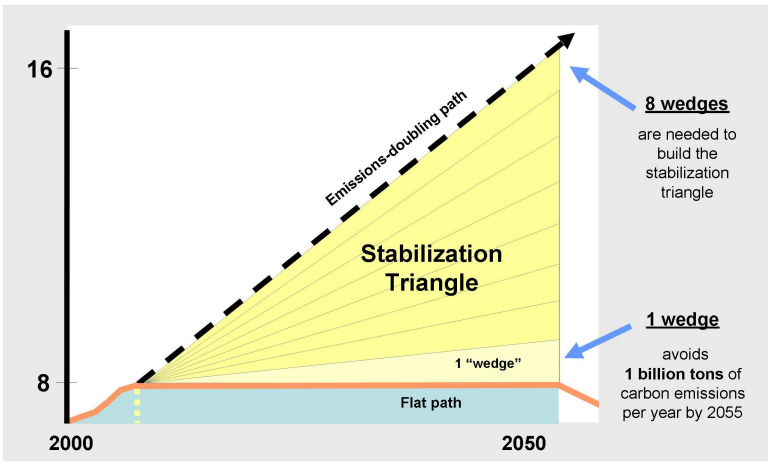

(b)

Figure 2.2: The historical and future CO_2 emissions as predicted by the Carbon Mitigation Initiative (a) and a magnification of the stabilization triangle (b). Source CMI[12].

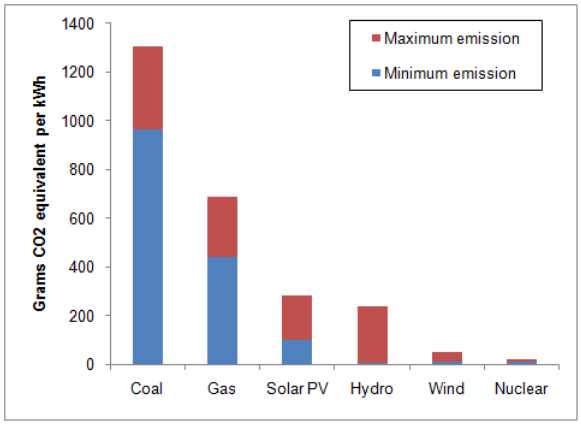

Figure 2.3: CO_2 emissions from traditional means of energy supply. Source: IAEA [13].

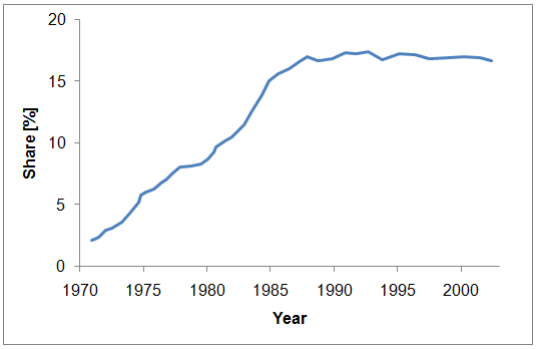

Figure 2.4: The share of nuclear power in produced electrical energy worldwide (percentage). Source: IEA [10]

committed to gradually phasing out the use of nuclear energy over the coming decades [14].

Nevertheless, the share of nuclear power in electricity production worldwide has not changed much since the end of the 1980s. As becomes clear from figure 2.4, the proportion of nuclear power in the electricity mix has stabilized at around 16%. In Europe, this number is around 35%, mainly due to heavy reliance on nuclear power in France. At the moment, 436 nuclear power reactors are in commission and 43 new reactors are under construction, partly as a replacement for reactors that will shortly be decommissioned [14]. Most notably, eleven new construction sites are found in China, which additionally has concrete plans for another 26 reactors in the near future.

As a result, we can conclude that although nuclear power has not been 'in fashion' over the last decades, nuclear power still supplies a significant part of electricity worldwide. A part that we cannot just replace by other means of electricity generation, in the light of the aforementioned developments.

2.4 Is nuclear power sustainable?

After considering the information in the previous sections, a first concluding remark we can reasonably make is that it is unlikely that nuclear fission as a means of electricity production will disappear in the near future, regardless of its aptitude as a long term sustainable solution, simply because we have no way of compensating its contribution to the energy mix. This is, however, completely unrelated to the question if nuclear power *should* disappear. Due to the fact that nuclear technology is a mature technology with a low CO_2 impact and is also still developing rapidly, it seems far more likely that nuclear power generation will be part of any energy solution for the foreseeable future. For this reason, it is expected by the International Energy Agency that the share of nuclear power generation will rise over the next decades [7].

We may have concluded that nuclear power is unlikely to disappear, but that does not yet answer the question of sustainability. To be sustainable, it should - to quote the most widely used definition of sustainability - "meet the needs of the present, without compromising the ability of future generations to meet their own needs." This is usually called the Brundtland definition of sustainability. It can be divided into three separate topics: environmental, economic and social sustainability.

So what does this definition imply for nuclear power? Is it sustainable? In the strict sense of this definition, the answer is probably no. Although there have been many significant improvements recently and a lot more can be expected in the near future, problems of dealing with the waste and proliferation issues are still present for example. But then again, according to the same definition, practically none of our current power generation methods is sustainable either, including the ones called renewables. An example we have already encountered in figure2.3, is solar photovoltaic conversion of energy, which still produces a relatively large amount of CO_2 over its complete lifecycle. Other examples are the current use of biomass, which cannot possibly be called socially nor environmentally sustainable due to its competition with food production and extensive deforestation to make room for plantations, and the application of hydro power, which is often questionable from a sustainable point of view as a result of large scale flooding of natural areas and the associated risk of dam failure to people living downstream.

Eventually, many methods have the potential to become sustainable methods of power generation, but perhaps so does nuclear power. The reality is that we are still a very long way from the sustainability of anything. Since the challenges described in the last sections are presenting themselves today, the best thing to do is compare the alternatives and indicate the direction of sustainability. To put it more popularly: We cannot simply burn coal until we find the ultimate sustainable solution. Returning to figure 2.3, we can rightly say that as a contribution to the reduction of CO_2 emissions, nuclear power is more sustainable than most other means of power generation. In that sense, eliminating nuclear power as an option might in fact be a very unsustainable thing to do. In other respects, however, it might be a sensible decision. We will have to make decisions about the application of the different alternatives based on which matters are more pressing and in what way we can move as far in the

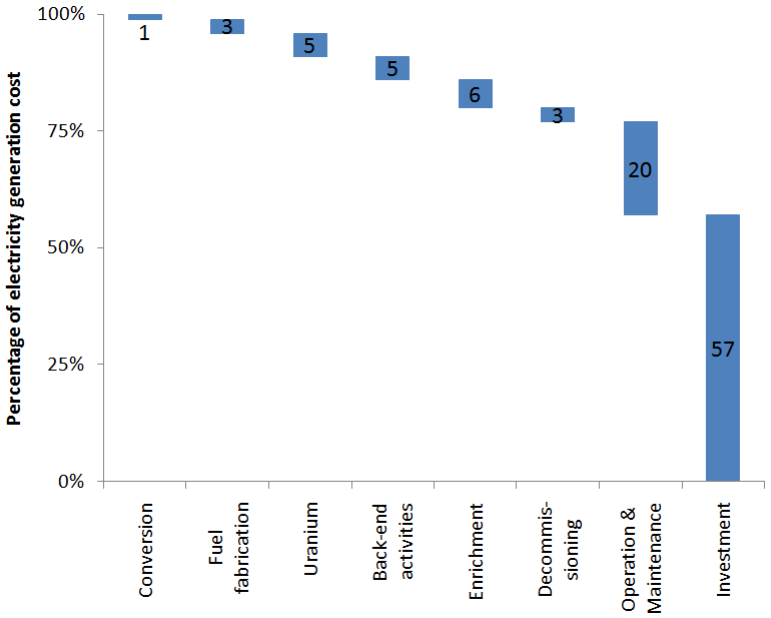

Figure 2.5: A breakdown of the typical buildup of the nuclear electricity generation cost [15].

direction of sustainability as we currently can.

As a result of the discussed trends, we can conclude that there will very probably be a need for more sustainable nuclear energy in the near future. In the meantime, we can improve the sustainability of existing nuclear power generation by conducting research and designing new reactor types. The ESBWR design is an example of the improvement of the social (safety) and economic sustainability of Boiling Water Reactors. These themes will therefore be discussed in a little more detail in the next sections.

2.5 Improvements to sustainability by the ESBWR concept

2.5.1 Economics

Nuclear power plants are very capital intensive. In contrast to most other fuel consuming means of power production, it is the initial investment that mostly determines the eventual price of electricity. In figure 2.5, a breakdown of the typical cost of nuclear electricity generation is shown. The large amount of financing required for building a reactor makes that it has to be slowly amortized over its lifetime. This means that the characteristic time window involved with the economics of new commercial nuclear power installations can be as long as 60 years in some cases. As a result, construction is only feasible if long-term competitive electricity prices can be guaranteed. Every effort to reduce the

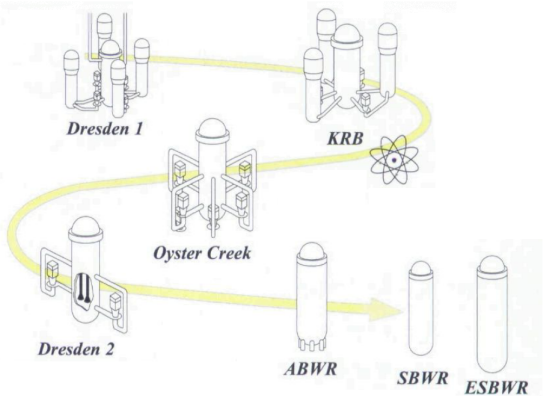

Figure 2.6: The increasing simplicity of the Boiling Water Reactor Design.

initial investment, while maintaining safety, is therefore a welcome improvement in this respect.

In the past, nuclear power generation has shown to produce electricity at a competitive price, but many of the safety improvements in new facilities, have come at extensive financial cost, contributing to an even higher initial investment cost. The great improvement of the ESBWR design is that it decreases construction and operational costs, while at the same time further improving the safety of the reactor.

Due to the fact that the ESBWR only uses natural circulation to drive the flow through the core, the design of the reactor vessel can be more simple than with more traditional designs (as schematically displayed in figure 2.6. The simpler design results in a reduction of initial investment due to lower production cost of the vessel and the fact that circulation pumps and the associated piping, control and safety measures can be left out completely. In addition, costly pump maintenance programs are no longer necessary. It is therefore expected that these improvements will significantly increase the economic feasibility of BWR power generation.

2.5.2 Safety

Much of the research concerned with the development of nuclear reactors has traditionally focused on safety. Catastrophical events in the past have contributed to this strong focus and although these events occurred in facilities that are uncharacteristical for modern western nuclear plants, safety remains - and righly so - a strong emphasis in today's social, political and research agendas. For sustainable application, referring to the Brundtland definition in section 2.4, it must be made sure that nuclear power will not form any long-term risks for society and the environment. The associated current 'sustainable direction' would therefore be bringing the safety of reactors within acceptable limits. In addition, the application of nuclear power generation in the energy mix is highly related to the level of public acceptance, in which safety considerations

Reactor design	maximum core damage frequency (yearly)
BWR/4	$1 \cdot 10^{-5}$
BWR/6	$1 \cdot 10^{-6}$
ABWR	$2 \cdot 10^{-7}$
ESBWR	$3 \cdot 10^{-8}$
AP1000	$5,09 \cdot 10^{-7}$
EPR	$6,1 \cdot 10^{-7}$

Table 2.1: Maximum core damage frequencies for several Boiling Water Reactor designs and two modern Pressurized Water Reactor designs: The AP1000 and the European Pressurized Reactors. [6].

are a major driver. One of the most important aspects of the sustainability of nuclear reactors will therefore be their safety.

Along with many other improvements, the generation of nuclear reactors that has recently become available on the market, boasts passive safety measures. This means that no active intervention is necessary to guarantee the safety of the reactor. The ESBWR also belongs to this new generation. As natural circulation drives the flow, removing the heat from the core does not require operator action anymore. As a result, cooling of the core is guaranteed under all conditions. The difficulties start, however, if we try to quantify the acceptability to society. One way to do this, is by conducting a risk assessment. In table 2.1, the calculated maximum core damages frequencies that are part of the extensive risk calculations required for the approval of a new reactor type, are displayed. This number is a term used in the risk assessment to indicate the likelihood of an event that would cause maximum damage to the core and possible discharge of radioactive material to the environment. From the figures in the table, it becomes clear that the likelihood of a major incident in the ESBWR is significantly decreased compared to earlier BWR designs like the BWR/4, BWR/6 and ABWR that are presently in operation. Also in comparison to modern Pressurized Water Reactors, on which construction has begun in China and Finland, the ESBWR boasts significant improvements in this respect.

Nevertheless, can these risks be deemed acceptable? One thing we can do is compare the maximum core damage frequency figures to other major events that would result in similar, or worse consequences to society. Dams for hydroelectric power generation, for example, have a calculated average failure rate of 10^{-5} per year [16, 17]. In populated areas this could have severe consequences, as multiple events in the past have already shown [14]. An example that might be more apt for Delft, is the estimated failure rate of coastal protection. For the province of South-Holland, the probability of severe flooding incidents causing an estimated death toll of thousands, is around $4 \cdot 10^{-4}$ yearly [18].

More quantitatively, this comparison can be formulated using the concept of risk, which is defined as the probability of an event occurring (P) times the impact of that event (I). In the form of an equation:

$$R = P \times I$$

If we leave the damage to economy out of the comparison, the flood risk can

be calculated to amount to $0,23$ casualties per year [18]. It is hard to estimate the impact of a nuclear incident. But even if we range the impact in thousands of casualties, which is a highly exaggerated number, the risk will still be three orders of magnitude smaller.

Of course, many comments can be made in regard to this approach, but the simple fact remains that the ESBWR design brings the risk associated with the application of nuclear power to unimaginably low numbers. In practice we can therefore conclude that the ESBWR design answers the need for short-term, sustainable nuclear power.

Chapter 3

The CIRCUS experimental facility

3.1 CIRCUS configurations

To simulate the conditions occurring in the ESBWR during startup of the reactor, there was a need for a scaled facility to conduct experiments with. For this purpose, the CIRCUS facility was constructed. The present CIRCUS setup is in fact the third, modified setup. Originally, it was constructed as a single channel system, but it was later fitted with double and even four parallel channels to facilitate the investigation of the effect of chimney division on reactor stability. For the remainder of the report, these different configurations will be referred to as CIRCUS I, CIRCUS II and CIRCUS IV respectively. The total cross-sectional surface area of the channels was kept approximately the same to simulate the division of a single riser into several sections, as can be seen in figure 3.1. The core section was left unchanged in each configuration.

The exact measures for the different configurations can be found in table 3.1. Detailed descriptions of the first two CIRCUS set-ups are provided by Manera [4] and Marcel [5], whereas the CIRCUS IV facility, the implementation of void detection and certain aspects of the calibration of the setup will be discussed in the next sections.

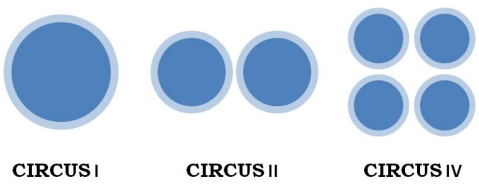

Figure 3.1: The total cross-sectional area of the chimney sections in the different CIRCUS configurations, viewed from the top.

	Circus I	Circus II	Circus IV
Chimney diameter	47 mm	33 mm	$24,4$ mm
Chimney cross-sectional area	$1,73 \cdot 10^3$ mm^2	$8,55 \cdot 10^2$ mm^2	$4,68 \cdot 10^2$ mm^2
Total chimney cross-sectional area	$1,73 \cdot 10^3$ mm^2	$1,71 \cdot 10^3$ mm^2 (-1%)	$1,87 \cdot 10^3$ mm^2 (+8%)
Core inner diameter	$20,4$ mm	$20,4$ mm	$20,4$ mm
Heating rod diameter	$12,5$ mm	$12,5$ mm	$12,5$ mm
Core cross-sectional area	$2,04 \cdot 10^2$ mm^2	$2,04 \cdot 10^2$ mm^2	$2,04 \cdot 10^2$ mm^2
Downcomer diameter	51 mm	51 mm	$25,5$ mm
Bypass Channel diameter	10 mm	10 mm	10 mm
Core length	2038 mm	2038 mm	2038 mm
Chimney length	3068 mm	3068 mm	3559 mm
power range per rod	0 - 3 kW	0 - 3 kW	0 - 3 kW
Pressure range	1 - 5 bar	1 - 5 bar	1 - 2 bar

Table 3.1: Relevant characteristics of the different CIRCUS configurations.

3.2 Circus IV

The CIRCUS facility in its current configuration is shown schematically in figure 3.2. Besides having four parallel channels, there are a few other differences between CIRCUS IV and its predecessors. The pressure vessel that was present in the previous setups, has been removed and the steam dome is placed directly on top of the chimney exit. Also, a pre-heater has been installed near the core inlet, that can be used, when necessary, to more accurately set the temperature of the water entering the core. As indicated in table 3.1, CIRCUS IV is somewhat taller than its predecessors. This is due to the fact that the top of the chimney section was rebuilt in a slightly different configuration to accommodate for four parallel channels. In addition to this, it was fitted with extra valves to be able to impose an exit friction.

For the rest, the setup has largely remained the same. Each of the four chimneys is installed on top of a separate channel that contains an electrically heated rod. Each rod can be set to deliver a power from 0-3 kW to the surrounding water. Below the core inlet, a set of valves is included, which makes it possible to add friction to each channel separately or to close off channels completely. Over this part of the setup, differential pressure sensors have been installed, capable of measuring both negative and positive pressure drops.

3.3 Thermocouple calibration

At the start of this project, it was made sure that all thermocouples were inserted into the flow at exactly the same distance, i.e. 5 mm from the inner wall of the channels. Subsequently, all thermocouples in the setup were calibrated against the PT100 at the central inlet below the core. This is done by recording the cooling down of the setup under forced flow conditions. The acquired curves for each thermocouple and the PT100 are then fitted with a second order polynomial curve in Matlab. The thermocouple signals are then adjusted for their deviation

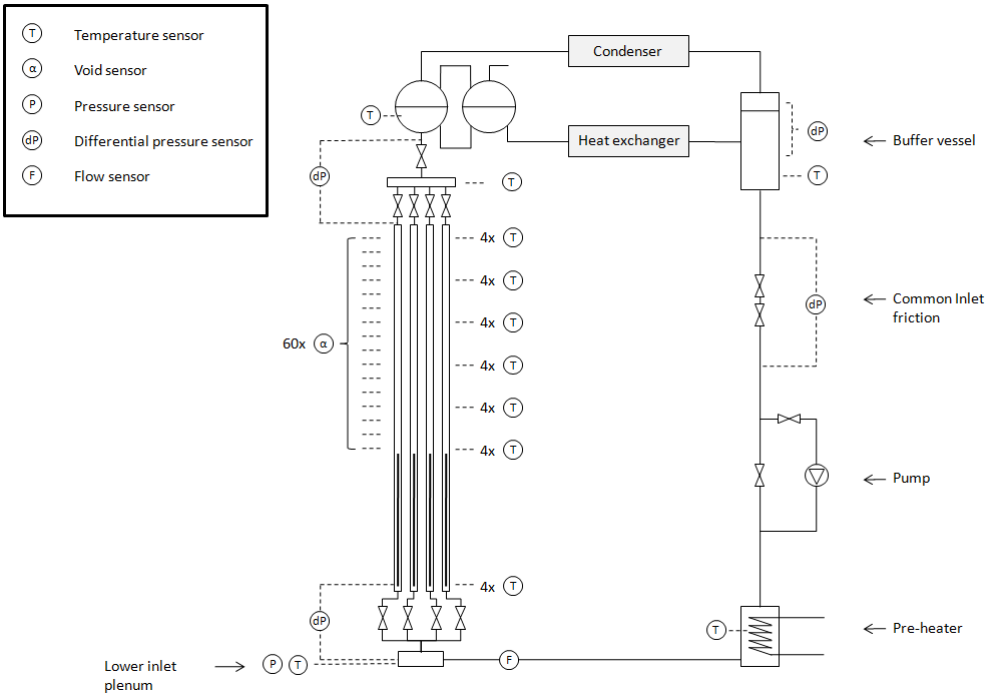

Figure 3.2: A schematic version of the CIRCUS experimental setup.

from the PT100 fit.[1] After correction, all thermocouple signals are found to be within a range of approximately 0,5 K. The calibration results can be found in appendix B. In turn, the PT100 at the inlet is calibrated manually by detaching it from the setup and measuring its response signal while keeping it in melting ice and boiling water at known atmospheric pressure.

3.4 Partial flow measurement

For a detailed investigation of the instability phenomena, we are not only interested in the flow through the primary circuit, measured by the flow meter at the bottom of the setup. It will also be useful to determine the partial flows, i.e. the flow through each of the four channels separately. Using the differential pressure sensors at the inlet channels below the core, this partial mass flow through the channel can be calculated using te following relation:

$$M_i^2 = \frac{2A^2\rho}{K_{in,i}}\Delta p_i \tag{3.1}$$

where Δp_i is the measured pressure drop over each inlet channel, $K_{in,i}$ the local friction coefficients in the corresponding channels and M_i the mass flow through each channel. Most of this analysis has been done by Weppelman [19].

[1] This has been done before by Weppelman [19], but at that point the radial positions of the thermocouples in the channels were unknown and insulation had not yet been added to the setup.

	$K_{in,i}$
Inlet channel 1	$3,54 \pm 0,14$
Inlet channel 2	$3,42 \pm 0,12$
Inlet channel 3	$3,43 \pm 0,12$
Inlet channel 4	$3,38 \pm 0,14$

Table 3.2: The friction coefficients related to the valves and bends in the inlet channels below the core.

Due to the large measurement range of the differential pressure sensors and as a result of thermal effects on the arrangement of the pressure sensors, Weppelman found that uncertainties in the determination of the pressure drop are approximately 130 Pa. For certain conditions this is too large to calculate a sensible value for the mass flow, for example for single phase natural circulation conditions, with typical pressure drops below 100 Pa. On the other hand, for larger mass flows, as during flashing or reverse flow phenomena, calculation with small relative uncertainty is possible.

3.5 Local friction coefficients

Relation (3.1) is also used to determine the friction coefficients of certain parts of the facility. For example, to facilitate easier comparison to the previous setups, the common inlet friction coefficient, K_{in}, is manually set to a comparable value by means of adjusting a valve in the downcomer.[2] Afterwards, the friction coefficient is calculated by recording the pressure drop over the relevant part of the setup for a range of different mass flows and applying equation (3.1). All friction coefficients have been determined in high (forced) flow conditions. Due to the comparatively low contribution of the channel wall friction to the pressure drop in these conditions, the latter has been neglected in the determination of the local friction coefficients.

In this case, the inlet friction coefficient was set to $K_{in} = 8,9$, a value close the the value used by Marcel [5] ($K = 8,65$). This friction was left unchanged during measurements, unless indicated differently. In the same way, the friction coefficients for the inlet valves have been previously calculated by Weppelman [19]. In table 3.2, the values for these frictions can be found. The central exit friction, which is caused by the recombination of the four channels at the top of the chimneys, was found to be $K_{ex} = 1,7$.

3.6 Void measurement

For a thorough understanding of the phenomena occurring in the chimney sections, it is of interest to know the (axial) location of void production and collapse. In the preceding CIRCUS setups, this was achieved by applying wire-

[2] The position of the inlet friction valve is indicated in figure 3.2.

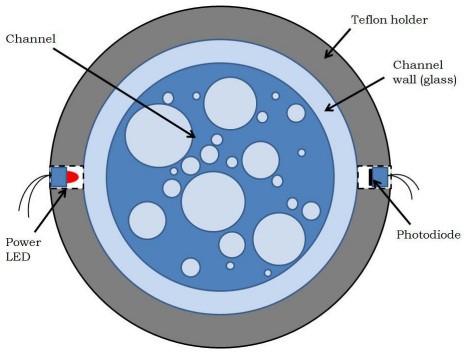

Figure 3.3: One void sensors attached to the set-up (top view).

mesh sensors, gamma-transmission techniques and conductivity needle probes.[3] Unfortunately, each of these methods has its disadvantages and are not applied to CIRCUS IV due to practical considerations or simply because it became too costly to implement enough of them for a complete picture about void production in a setup with four separate chimneys.

Instead, a simple optical sensor was developed and implemented as a part of this project. It was shown to produce good results in the detection of void passing through the chimneys. A total of 60 of these simple optical void sensors have been installed at regular intervals on the outside of the glass chimney sections (15 per chimney). The sensors consist of a focused red power-LED and a photodiode, embedded into a teflon ring, on opposite sides of the glass channel wall. The technical specifications of these sensors can be found in appendix E. In figure 3.3, a single sensor is depicted schematically and in figure 3.4, two photographs of the sensor array attached to the set-up is displayed. Since an insulating foam layer will cover the installed sensors during experiments, noise from surrounding light sources on the photodiode signal is eliminated.

When a vapor bubble passes the bundle of red light in the channel, it briefly disrupts it due to the refraction of the light at the bubble boundary. This causes a sharp decrease in the photodiode signal. It is clear that a sensor of this type is only able to indicate the presence of vapor in the chimney rather than the vapor fraction. A typical output signal from the photodiode is shown in figure 3.5 (top). The downward fluctuations of the signal indicate the presence of vapor at the location of the sensor. The upward fluctuations of the signal in this case are due to the applied filter during data collection. Directly below the photodiode data, the temperature in the chimney at approximately the same axial location is displayed to provide an idea of the conditions in the chimney over time.

As indicated in the magnifications in figure 3.5, the sensors clearly capture both the fast signal fluctuations associated with bubbly flow (in magnification (a)) and the larger void flashing and geysering events (magnification (b)). Although the signals in the magnifactions look quite noisy, the registered peaks can completely be attributed to vapor passing in the chimney. The noise level itself is

[3] More information about the applied techniques can be found on pp. 7-13 in [4] and on pp. 77 in [5]

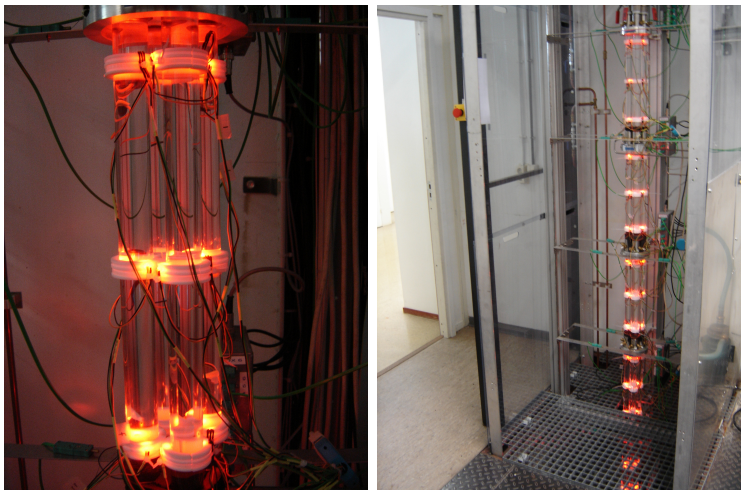

Figure 3.4: A set of pictures of the array of void sensors attached to the CIRCUS IV set-up.

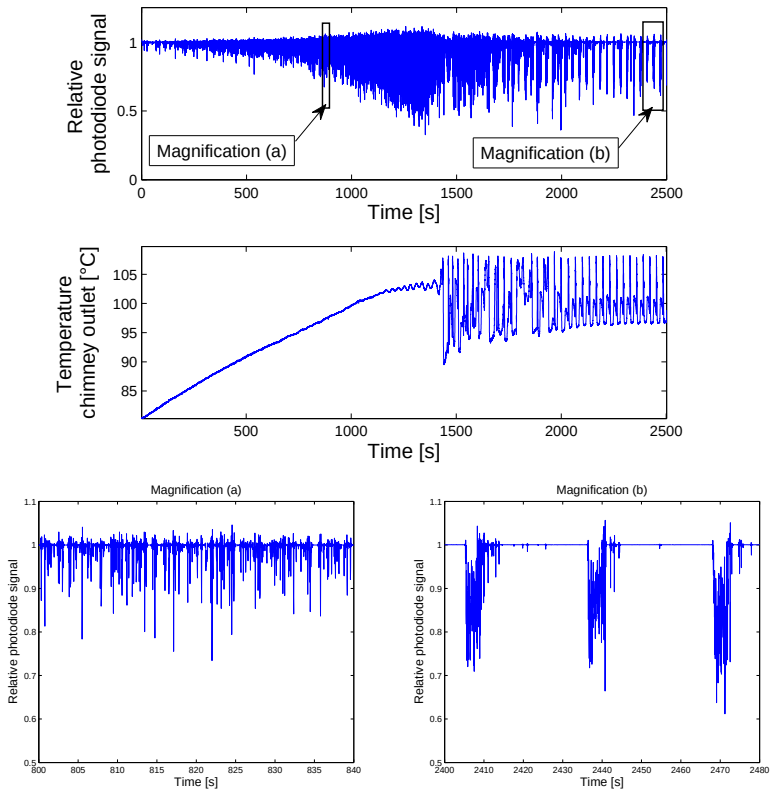

Figure 3.5: Void sensor data (top) and the temperature at the chimney outlet (centre) after starting up the Circus IV facility at full power (11 kW), as well as magnifications of the void sensor signal for the indicated domains (bottom).

only 0,5% of the photodiode signal.

The array of LED-Photodiode Sensors is used to determine the axial position of void in the riser sections. The signal received from the photodiodes is registered by a separate computer system at 1000 Hz per channel. Synchronization of this system with the regular data acquisition system in CIRCUS IV (which registers all other observed parameters) is conducted by applying a manual trigger signal to one input channel in each system. A number of Matlab scripts have been written to process the photodiode signals.

To test the agreement of the photodiode signals with the vapor in the chimney sections, high speed camera images were recorded during flashing phenomena. The data recorded by the sensor was shown to correspond very well to the individual bubbles passing the sensor in the chimney. Although the information from the sensors has, in the course of this Master project, only been used to determine the location of void production and the direction of the vapor flow, the detailed detection of individual bubbles and the distinct differentiation between the two magnified signals provides hope for a possible future determination of flow regimes based on photodiode data. It is expected that bubbly, slug and churn flow can be individually detected on the basis of characteristic signals from the void sensors.

3.7 Heat loss

To limit heat losses to the surroundings, foam insulation has been wrapped around the four chimney sections, as was also done with the CIRCUS I and II chimneys. Nevertheless, there is still some heat loss, although it will be hard to estimate due to the irregular shape of the facility. At a water temperature inside the facility of approximately 99 °C, the outside of the foam reaches an average temperature of 35,9 °C in surroundings of 28 °C.

This means that the heat loss in the chimney is very small compared to the heat loss in the core. The core section is not insulated and the four glass channels containing the heating rods are open to the surrounding air. Since the flow in the core sections has been turbulent during all measurements conducted in the CIRCUS IV facility, we will neglect the heat transfer coefficient from the water to the glass wall and assume that the inside of the wall is at the same temperature as the water.[4] We can therefore estimate the heat loss in the core by applying Fourier's law in cylindrical coordinates to the glass wall:

$$\phi'' = -\lambda \frac{dT}{dr} \tag{3.2}$$

[4] A quick estimation of the heat transfer coefficient shows that this assumption is acceptable. If we approximate the glass pipes as a flat wall, we can calculate the overall heat transfer coefficient as follows:

$$\frac{1}{h_{tot}} = \frac{d_{bl}}{< Nu > \lambda_{H20}} + \frac{d_{wall}}{\lambda_{wall}}$$

Where the Nusselt number in the core varies between 20 and 75 for CIRCUS IV operational conditions (and is even higher during forced flow). Since the thermal boundary layer, d_{bl}, is at most of the order of the channel width, we see that the first term becomes much smaller than the second. Neglecting the resistance to heat transfer from the water to the glass is therefore allowed.

or

$$\phi = -\lambda A(r)\frac{dT}{dr} = -\lambda 2\pi r L\frac{dT}{dr} \tag{3.3}$$

If we rewrite the equation to isolate the differential:

$$\frac{dT}{dr} = -\frac{\phi}{\lambda 2\pi r L} \tag{3.4}$$

and integrate from the inside of the glass wall R_1 to the outside, R_2, we get

$$T_1 - T_2 = \frac{\phi}{\lambda 2\pi L} ln\left(\frac{R_2}{R_1}\right) \tag{3.5}$$

where evidently T_1 is the temperature at the inside of the glass tube and T_2 at the outside. In a forced flow conditions, with a constant average water temperature of 95,1 °C, the average outside wall temperature is measured to be 92,2 degrees, with a wall diameter of 3 mm. Using equation 3.5, we can calculate that this amounts to a total heat loss of approximately 1500 W over the four core sections. Radiation heat losses can be neglected in comparison to this number. We must be aware, however, that assuming these temperatures to be constant is quite a stretch during regular operation.

Chapter 4

Phenomenological description

This chapter will deal with the description of the instability phenomena encountered in the CIRCUS IV facility. First, the instability phenomena will be classified on the basis of their phenomenology and organized into a reference map in the power-subcooling plane, the so called stability map. This map will subsequently be compared with stability maps created for the CIRCUS I and II setups. From this comparison, we will be able to draw some first conclusions on the influence of chimney division on stability.

4.1 Stability behavior

Depending on the conditions in the facility, six different kinds of stability behavior are encountered in CIRCUS IV. These behaviors have mainly been classified on the basis of the flow in the primary circuit. For example, if we fix the power applied to the heating rods in the core and simply have a look at the primary flow through the facility while slowly increasing the inlet temperature, we obtain the mass flow characteristics displayed in figure 4.1. In order of appearance from left to right (so from high subcooling to low subcooling) we encounter: High subcooling stable flow, in-phase flow oscillations (also called intermittent oscillations), a-periodical oscillations, out-of-phase oscillations, higher order out-of-phase oscillations and low subcooling stable flow. The transition to the low subcooling stable flow was not experimentally detected in low inlet friction conditions (although the state itself was[1]) and is therefore estimated in figure 4.1 for the sake of completeness.

If we compare the observed regimes with the ones found by Marcel [5] in CIRCUS II, we see that one type of unstable behavior has been added: the higher order out-of phase oscillations. Although at first sight this behavior might not seem very different from the regular out-of-phase oscillations, we will see in section 4.1.5 that the oscillation is caused by different phenomena. We will also see that more differences have been found with respect to the instabilities in CIRCUS

[1] In section 4.1.6 it is explained how the low subcooling stable flow state can be achieved in the measurable range, while the transition to this state cannot be exactly determined.

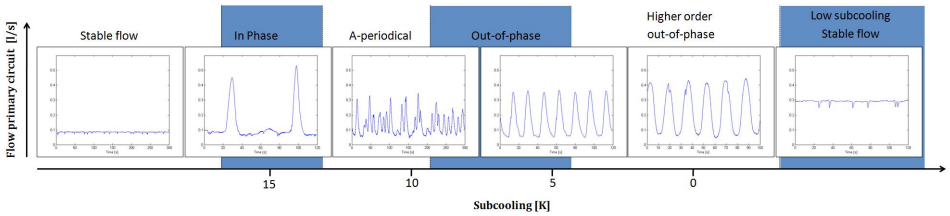

Figure 4.1: The primary mass flow signal in different stability regimes at $P = 2200\text{W/rod}$ and $K_{in} = 8,9$. The low subcooling stable flow boundary is estimated.

	t_1	t_2	t_3
Ch. 1	F	$\downarrow$	F
Ch. 2	$\downarrow$	G	$\downarrow$
Ch. 3	$\downarrow$	G	$\downarrow$
Ch. 4	$\downarrow$	G	$\downarrow$

Table 4.1: An example of a timetable used to describe the instabilities occurring in the setup.

II and that the configuration of the regimes in the power-subcooling plane is quite different. All stability regimes and their characteristics, are described in the next paragraphs.

Before continuing to the description of the instabilities themselves, one conclusion about them is best explained at this point. All of the observed instability behaviors can be considered to be caused by three main phenomena: Flashing, geysering and reverse flow. Two of these phenomena, flashing and geysering, have been explained in the introduction. The last one, reverse flow, is defined as a flashing- or geysering-induced reverse mass flow in one or more of the channels. Since the description and especially the explanation of the instabilities is often not straightforward, time tables will be applied to clarify which of the three phenomena plays a role at what point in time. An example of such a table is provided in table 4.1. The rows indicate the different channels in the setup, while the columns indicate moments in time that are of interest, but are not necessarily separated by an equal amount of time. The occurrence of the main phenomena are indicated by symbols. F for flashing, G for geysering and $\downarrow$ for reverse flow. For example, at t_1 we see a flashing event in channel 1 and a simultaneous reverse flow in channels 2-4. This tool will prove to be instructional while analyzing the process behind the different instabilities.

4.1.1 High subcooling stable flow

At relatively low inlet temperatures, there is only very little production of vapor in the system. In this case, the system displays no mass flow oscillations due to void flashing, as can be clearly seen in figure 4.2a. The small downward peaks in the signal are caused by the flow meter itself and do not represent mass flow oscillations. The regime is characterized by identical axial temperature profiles

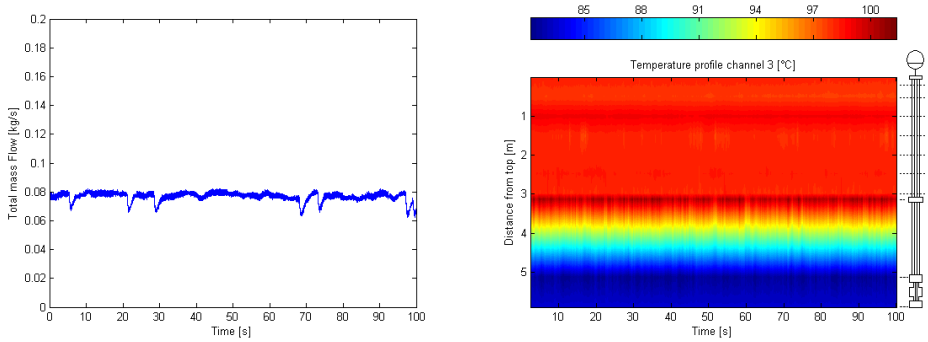

(a) (b)

Figure 4.2: The total mass flow (a) and the channel temperature profile (b) as a function of time (0 - 100 s) during high subcooling stable cirulation at $P = 1400\text{W/rod}$, $T_{sub,exit} = 15$ K and $K_{in} = 8,9$.

	t_1	t_2	t_3	t_4
Ch. 1	↓	G	↓	G
Ch. 2	F	↓	F	↓
Ch. 3	↓	G	↓	G
Ch. 4	↓	G	↓	G

Table 4.2: The events timetable for in-phase oscillations. Event t_2 follows event t_1 within seconds. The time span between t_2 and t_3 is very long.

in all channels, of which one is shown in figure 4.2b. There is no detectible void present in the chimneys.

4.1.2 In-phase flow oscillations

In the in-phase oscillation regime, all four channels display a flow oscillation at practically the same time. As we can see from figures 4.3c, a mass flow oscillation is initiated by a flashing event in *one* chimney (channel 2 in this case, indicated by point A in figure 4.3c). Due to buoyancy, the flow in this channel is strongly increased. As a result of the inertia of the large amount of water in the rest of the natural circulation loop and the local friction experienced by the flow in the downcomer, this flashing event is enough to cause a small reverse flow in the other three chimneys, or at least to halt the flow there. The temperature of the water in those chimneys, meanwhile, is not far from the saturation temperature. Since the flow is slightly reversed or halted in these channels, the already hot water in the core (or flowing back into the core), reaches the saturation temperature shortly after, causing a geysering event in at least one other channel, which is enough to bring the remaining channels to geyser quickly after that.

This is where the story ends for in-phase flow oscillations: although the three geysering channels also cause a reverse flow in the channel that started the event,

	t_1	t_2	t_3	t_4	t_5	t_6
Ch.1	F	↓	G	↓	F	↓
Ch. 2	↓	↓	G	↓	F	↓
Ch. 3	↓	G	↓	G	↓	G
Ch. 4	↓	G	↓	G	↓	↓

Table 4.3: An example of a timetable for behavior in the a-periodical regime. It must be emphasized that the events are not equally separated in time.

it has been flooded with relatively cold water from the channel inlet due to the large increase in flow during flashing, as can very clearly be seen in figure 4.3b (point B). Therefore, the reverse flow is not enough to cause another geysering event, stabilizing the flow until the next flashing event. As we will see in the next section, this is the defining difference between in-phase oscillations and non-periodical flow oscillations.

The In-phase flow oscillations observed in CIRCUS IV are similar to those found by Marcel [5] in CIRCUS II. In that case, it was also found that in-phase oscillations always start with a flashing event in one of the channels, which subsequently induces a geysering event in the other channel. It is interesting to see that in CIRCUS IV the oscillation is still induced by a flashing event in only one channel.

4.1.3 A-periodical flow oscillations

A-periodical flow oscillations are also caused by a combination of void flashing and geysering events, with the difference that there is no regular pattern anymore. As with in-phase oscillations, the oscillation starts with a void fashing event. However, after initiation of a flashing event in one chimney and the subsequent geysering in the other channels, the temperature in the core of the initial channel might now be high enough to cause a subsequent geysering event in that channel. Since this new geysering event will again generate reverse flow in the other channels, this effect could in principle sustain geysering in all channels indefinetely. Nevertheless, at a certain point in time, this cascade of geysering events will be perturbed just slightly (for example by a fluctuation in the inlet temperature or a smaller geysering event in one of the chimneys and thus a smaller reverse flow in the other channels). In that case, the temperature in the core will not be high enough to initiate a geysering event anymore and a flashing event will follow. It is therefore due to the random nature of these perturbations and the different time scales involved with flashing and geysering, that the a-periocial behavior arises. In table 4.3, an example of a timetable for a-periodical oscillations is shown.

In figure 4.4 such an alternation can be seen. We will follow the event, using the heat and void profiles in figures 4.4b and 4.4c, to get a clearer picture of what is happening. We see that the subsequent geysering events in channels 1 and 2 (indicated by A and B respectively), fail to induce a geysering event in channels 3 and 4 by reverse flow. As a consequence, the temperature build-up in those two channels starts showing similarities to the in-phase oscillations (indicated

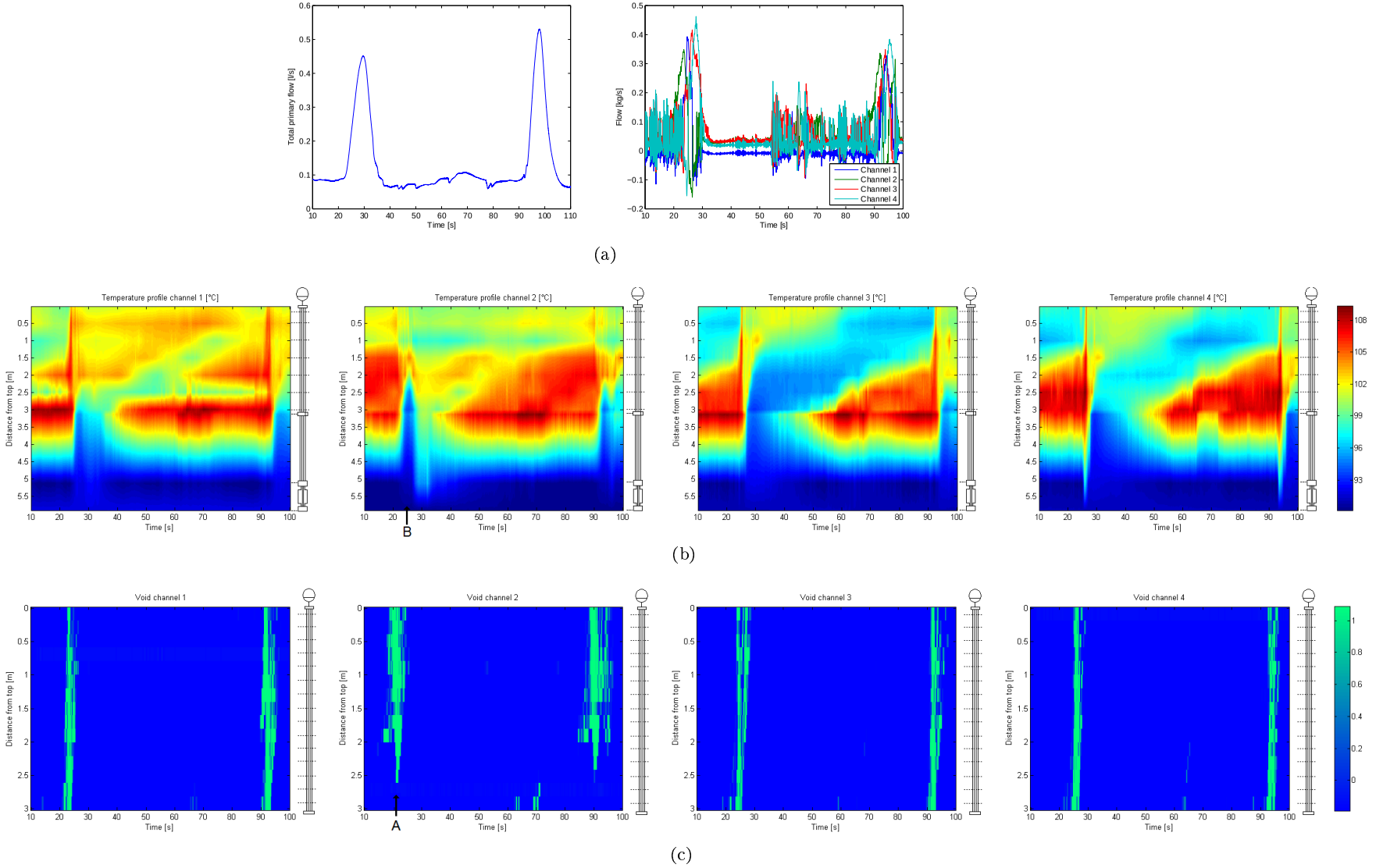

Figure 4.3: The total mass flow and the partial mass flow per channel (a), the temperature profiles (b) and void detection data (c) as a function of time for in-phase oscillation at $P = 1,4$kW, $T_{sub,exit} = 7,3$°C and $K_{in} = 8,9$. The time is indicated in seconds on the horizontal axes (10 - 100) and on the vertical axes the axial position of the sensor in question is given. This has been clarified by the schematic versions of the CIRCUS IV facility next to the pictures. Note that the temperature sensors are installed installed over the whole length of the setup, whereas the void sensors are only present in the chimney. From left to right, the images represent the channels 1 to 4, respectively.

by C). At point D, this results in a flashing event in channel 4, completely disrupting the regular cascade of geysering events that was in place before the beginning of the time scale. The unpredictable alternation of the geysering and flashing phenomena gives rise to the characteristically a-periodical mass flow oscillations.

Determination of the a-periodical behavior can be complicated in some cases. Cascades of geysering events can sometimes continue for a long time, especially at high power and low subcooling. As a consequence, the recorded signal often seems periodical. Increasing the inlet temperature causes these temporary periodical oscillations to persist even longer. When, at a certain point, no flashing events and subsequent distortions of the periodic signal are observed anymore in the measured timeframe (usually 3-5 minutes) , the signal is classified in the out-of-phase regime. This means that the determination of the a-periodical regime is limited by the measurement window.

This type of A-periodical behavior has also been found in the CIRCUS II setup by Marcel. He showed that the occurrence of a-periodical behavior may be seen as a cascade of period-doubling oscillation frequency bifurcations, which are impossible to discriminate from each other. This means that the a-periodical regime can be thought of as an oscillation frequency transition zone between the very distinct (but different) oscillation frequencies in the a-periodical and out-of-phase regimes.

A-periodical oscillations in high-inlet friction conditions

The a-periodical mass flow oscillations described so far, are of the type most commonly encountered during experiments. At high inlet friction conditions, however, another type of a-periodical behavior can arise. At these conditions, the reverse flow can become large enough to cause hot coolant from one channel to pass through the lower inlet plenum to another channel. As a result, the temperature of the coolant directly after a geysering event in a channel, is higher than it would be if it were only flooded with relatively colder coolant from the downcomer. The incubation time for the next geysering event in the same channel will therefore be shorter, disrupting the 'rhythm' of the oscillation. As we have seen before, the random perturbations in the magnitude of the reverse flow, causes the a-periodical behavior.

Although the oscillations are only caused by geysering and reverse flow, they are definitely a-periodical. In figures 4.5a and 4.5b, the power spectral densities of this type of a-periodical oscillations is compared to the power spectral density of the (periodical) out-of-phase oscillations (described in the next section). It can clearly be seen that in the out-of-phase regime, oscillation occurs at a very distinct frequency (indicated by the arrow), whereas in the a-periodical regime a wide range of frequencies is found in the signal.

In table 4.4 an example of an oscillation timetable is displayed. At $t = t_2$ the reverse flow first passes through the common inlet, allowing channels 3 and 4 to geyser again, before channels 1 and 2 can. This gives rise to a-periodical geysering behavior. Bear in mind that the intervals between $t_2 - t_6$ are not regular intervals. This kind of a-periodical oscillation is very similar to some of

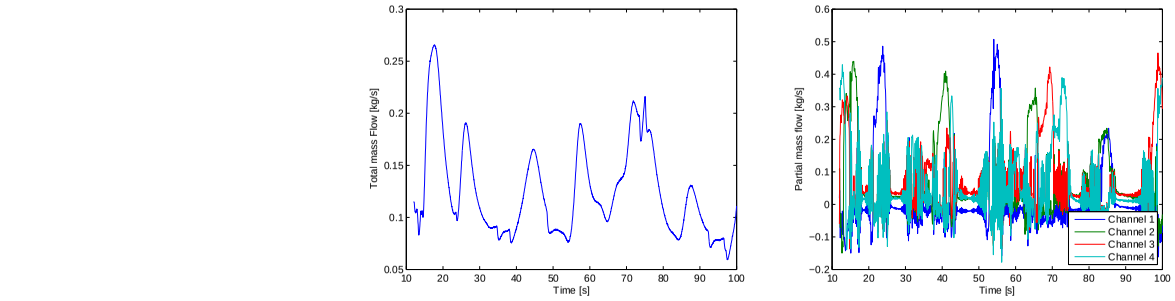

(a)

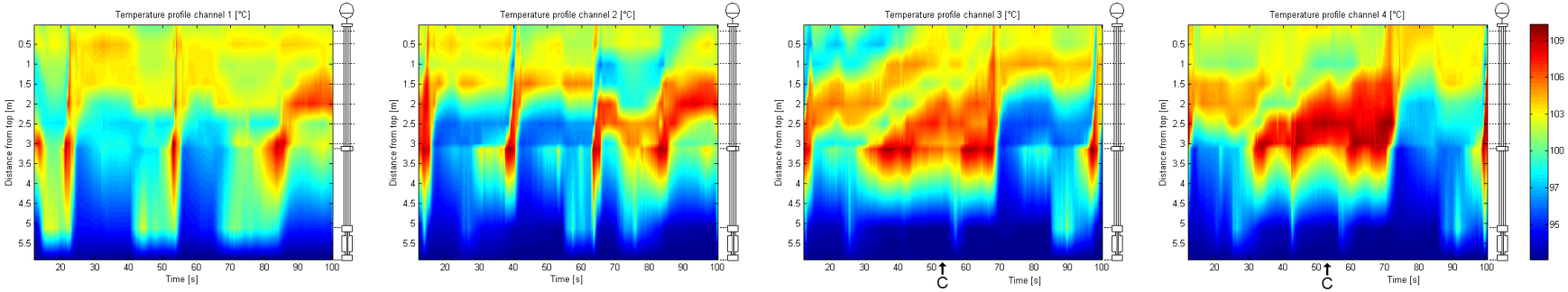

(b)

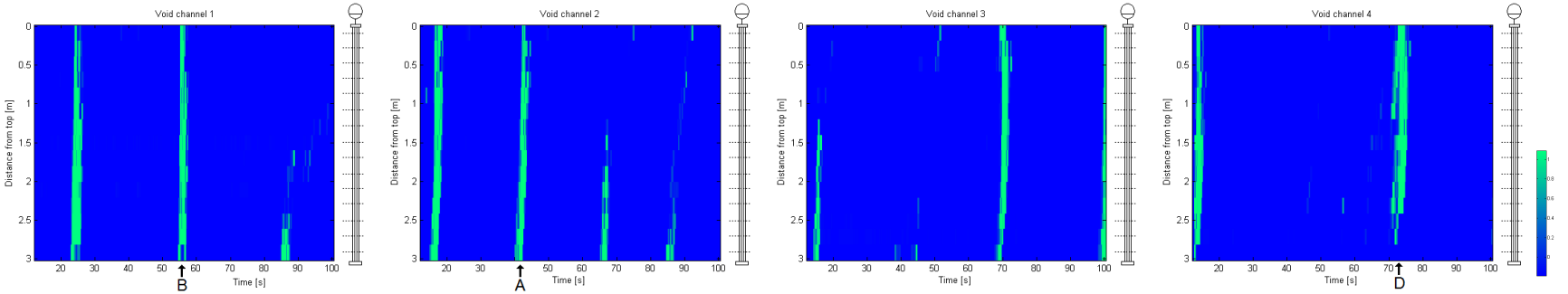

(c)

Figure 4.4: The Total mass flow and the partial mass flow per channel (a), the temperature profiles (b) and void detection data (c) for a-periodical oscillation at $P = 1,4$kW, $T_{sub,exit} = 5$°C and $K_{in} = 8,9$. The time is indicated in seconds on the horizontal axes (10 - 100) and on the vertical axes the axial position of the sensor in question is given. This has been clarified by the schematic versions of the CIRCUS IV facility next to the pictures. Note that the temperature sensors are installed installed over the whole length of the setup, whereas the void sensors are only present in the chimney. From left to right, the images represent the channels 1 to 4, respectively.

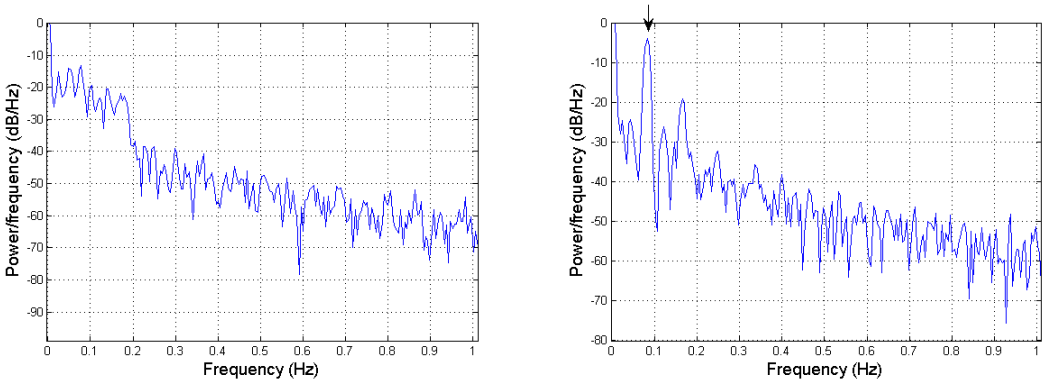

(a) (b)

Figure 4.5: The Power Spectral Densities of a mass flow signal from the a-periodical regime (a) and from the out-of-phase regime (b).

	t_1	t_2	t_3	t_4	t_5	t_6
Ch.1	G	↓	↓	↓	G	G
Ch.2	G	↓	↓	G	↓	↓
Ch.3	↓	G	G	G	↓	↓
Ch.4	↓	G	G	↓	↓	G

Table 4.4: High reverse flow a-periodical behavior timetable.

the higher order out-of-phase oscillations that will be described in section 4.1.5. The main difference is that the reverse flow in that regime occurs on a regular basis. Moreover, these two regimes are separated by another: the out-of-phase regime.

4.1.4 Out-of-phase flow oscillations

Continuing to an even lower subcooling domain in figure 4.1, we get to the regime where regular, sinusoidal oscillations are encountered. These oscillations are called "out-of-phase" because they typically involve the alternation of two chimneys displaying a geysering event and a reverse flow in the other two, as can be clearly seen in figure 4.6a. Whereas in the a-periodical regime, a periodical cascade of geysering oscillations could only be temporarily maintained, this is not the case in the out-of-phase regime. The oscillations in this regime always remain periodical, even after disturbing the power or friction in one or more channels. The oscillations in this regime are only caused by geysering and reverse flow. Flashing is not encountered anymore. This is a very distinct difference between the geysering/flashing-induced a-periodical oscillations, which will be very useful in the prediction of the stability boundaries between the regimes in chapter 5. The oscillation timetable is given in table 4.5.

The described oscillation is very similar to the out-of-phase behavior found by Marcel [5] in CIRCUS II. Even more so because of the two-by-two pairing of

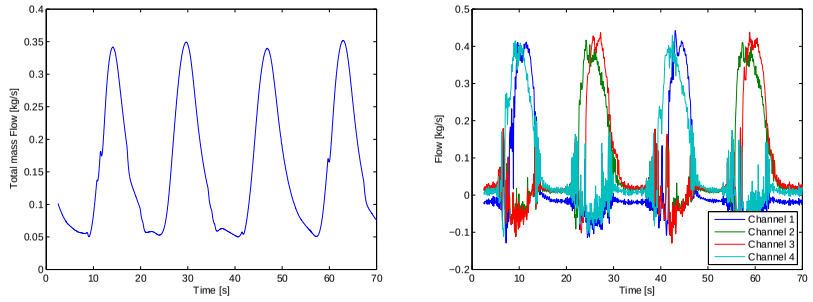

(a)

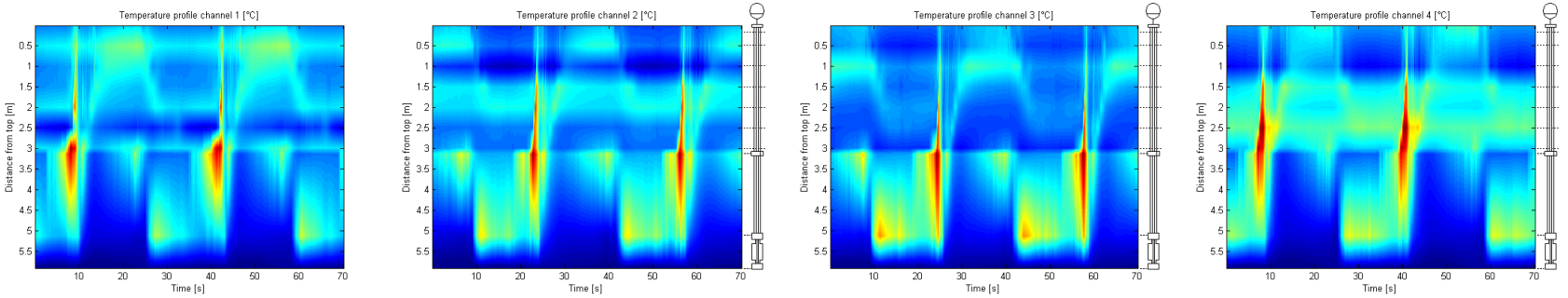

(b)

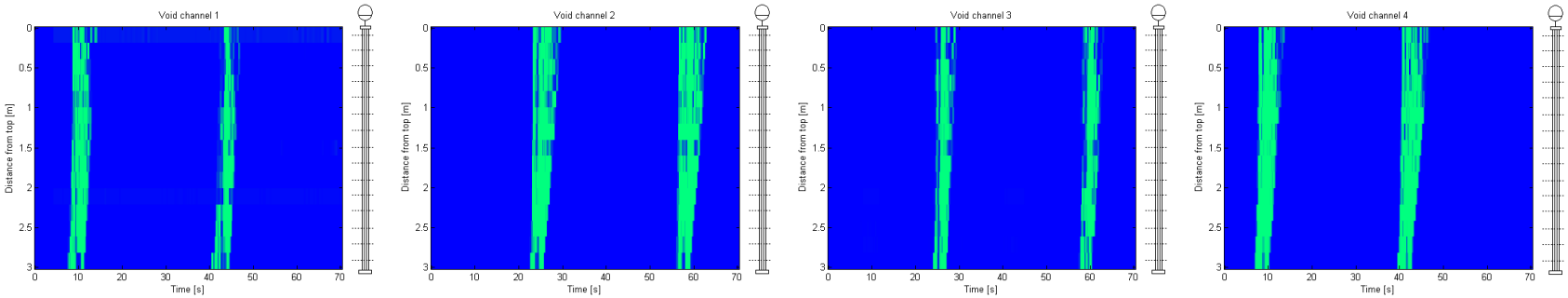

(c)

Figure 4.6: The Total mass flow and the partial mass flow per channel (a), the temperature profiles (b) and void detection data (c) for out-of-phase oscillation at $P = 1,4$kW, $T_{sub,exit} = 0,6$°C and $K_{in} = 8,9$. The time is indicated in seconds on the horizontal axes (0 - 70) and on the vertical axes the axial position of the sensor in question is given. This has been clarified by the schematic versions of the CIRCUS IV facility next to the pictures. Note that the temperature sensors are installed over the whole length of the setup, whereas the void sensors are only present in the chimney. From left to right, the images represent the channels 1 to 4, respectively.

	t_1	t_2	t_3	t_4
Ch.1	G	↓	G	↓
Ch.2	G	↓	G	↓
Ch.3	↓	G	↓	G
Ch.4	↓	G	↓	G

Table 4.5: The oscillation timetable for out-of-phase oscillations. In this case, the events are equally separated in time.

	t_1	t_2	t_3	t_4	t_5
Ch.1	G	-	↓	G	↓
Ch.2	↓	G	↓	G	↓
Ch.3	↓	↓	G	↓	G
Ch.4	↓	↓	G	↓	G

Table 4.6: The channel pairing process for out-of-phase oscillation, as suggested by the author. Events t_1 and t_2 occur at practically the same time, while the time spans between t_2, t_3, t_4 and t_5 are larger.

the geysering channels. An explanation for this pairing effect does not seem to be straightforward. It is speculated by the author, that the pairing is due to the fact that one geysering event does not induce a large enough reverse flow to postpone geysering in all other channels. This idea can be made clear when we have a look at table 4.6. At $t = t_0$ we turn on the power in the system. All channels will heat up at the same pace, but due to small perturbations one channel will always display a geysering event first (at t_1). Due to this event, there is a (small) equal reverse flow in all the other channels, pushing back hot coolant into the core. Shortly after, at t_2, one of the remaining three channels will display a geysering event, adding to the reverse flow in channels 3 and 4. At this point, the total reverse flow in those channels has been enough to push all the hot coolant from the core. After the two geysering events, the natural circulation brings the hot coolant back to the cores of channels 3 and 4 and at t_3 a simultaneous geysering event will follow. This, in turn, causes a reverse flow in channels 1 and 2 that is high enough to push the hot coolant from their cores. This way a two-by-two out-of-phase oscillation is achieved.

The pairing of the channels could be an interesting topic for further research, since it makes quite a difference in large multi-channel systems whether the geysering events are spread out in time, or display the same pairing behavior. In the former case, the total flow through the system will probably not vary far from its standard value, but if the channels start displaying a 10 vs. 10 or a 500 vs. 500 out-of-phase oscillation, this could have severe consequences for the mass flow.

4.1.5 Higher order out-of-phase flow oscillations

At even lower subcooling and high power, a regime was observed in which a range of more exotic oscillations can be observed. Most of them include states

	t_1	t_2	t_3	t_4
Ch.1	G	G	G	G
Ch.2	G	G	G	G
Ch.3	↓	↓	↓	↓
Ch.4	↓	↓	↓	↓

(a)

	t_1	t_2	t_3	t_4
Ch.1	G	↓	G	↓
Ch.2	G	↓	G	↓
Ch.3	↓	G	↓	G
Ch.4	↓	↓	↓	↓

(b)

	t_1	t_2	t_3	t_4
Ch.1	G	G	G	G
Ch.2	G	G	G	G
Ch.3	G	G	G	G
Ch.4	↓	↓	↓	↓

(c)

	t_1	t_2	t_3	t_4
Ch.1	G	↓	↓	↓
Ch.2	↓	G	↓	↓
Ch.3	↓	↓	G	↓
Ch.4	↓	↓	↓	G

(d)

Table 4.7: Oscillation timetables for some of the higher order out-of-phase oscillations. In all cases the interval between consecutive events is equal.

in which only reverse flow is detected in some channels and only geysering in other channels. Among the most important of the recorded oscillations are:

- Two periodically geysering channels in combination with only periodical reverse flow in the other channels (2 vs. 2 reverse, see table 4.7a).
- Geysering in two channels alternating with geysering in one other channel, combined with only reverse flow in the last channel (2 vs. 1 vs. 1 reverse, see table 4.7b).
- Three simultaneously geysering channels in combination with a simultaneous reverse flow in the last channel (3 vs. 1 reverse, see table 4.7c).
- All four channels geysering separately at equal time intervals (1 vs. 1 vs. 1 vs. 1, see table 4.7d).

In figure 4.7, for example, a 2 vs. 2 oscillation state is shown. From figure 4.7a, it becomes clear that there is a large reverse flow in channels 2 and 4 at each geysering event in the other channels. In this situation, the reverse flow has become large enough push all the hot coolant from the core sections of the none-geysering channels, as can be clearly seen from the downward slope in the temperature profiles at points A. This also means that hot coolant is inserted into the core of the geysering channels via the inlet, thus enabling them to reach the saturation temperature again before the reverse flow channels do. This way the oscillation is maintained.

Due to the fact that most of the oscillations in this regime are either linked to the presence of four parallel channels or occur only at high common inlet friction, the higher order out-of-phase regime was not observed in CIRCUS II.

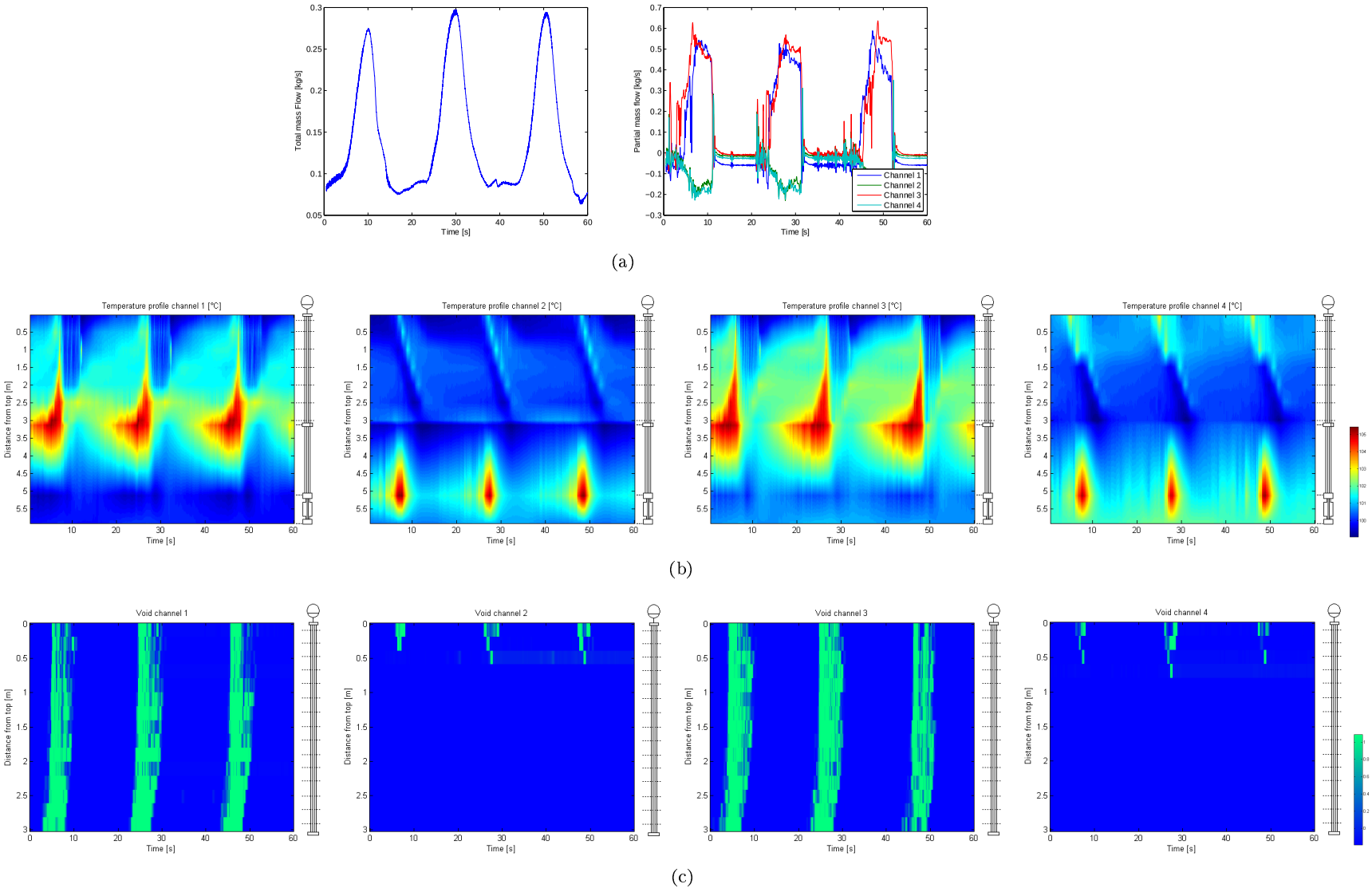

Figure 4.7: The Total mass flow and the partial mass flow per channel (a), the temperature profiles (b) and void detection data (c) for 2 vs. 2 reverse higher order out-of-phase oscillation at $P = 2,2\text{kW}$, $T_{sub,exit} = 0°\text{C}$ and $K_{in} = 8,9$. The time is indicated in seconds on the horizontal axes (0 - 60) and on the vertical axes the axial position of the sensor in question is given. This has been clarified by the schematic versions of the CIRCUS IV facility next to the pictures. Note that the temperature sensors are installed over the whole length of the setup, whereas the void sensors are only present in the chimney. From left to right, the images represent the channels 1 to 4, respectively.

4.1.6 Low subcooling stable flow

Inter-channel circulation

At very high power and low subcooling conditions, another stable mass flow regime emerges, as shown in figure 4.1. Although similar, it is not exactly the stable flow previously found in a single chimney setup by Manera [4] and Marcel [5]. In those cases, both a single phase as a two-phase region was present in the chimney, separated by a relatively stable flashing boundary. CIRCUS IV shows comparable behavior, but not for all chimneys equally. As we can conclude from the partial mass flow in figure 4.8a, continuous inter-channel circulation is present in the system at these conditions.[2] There are two stable flashing chimneys (channel 2 and 4 in this case), and two channels in which there is only a continuous reverse flow.

To clarify, we will have a look at the characteristics of a typical low subcooling stable flow in figure 4.8. The stable situation is initiated by a simultaneous geysering event in channels 2 and 4 (indicated as point A). During this event, the reverse mass flows in channels 1 and 3 become large enough to feed hot coolant from their cores to the inlets of the other two (already flashing) channels, which allows them to remain in a continuous flashing state. The example shown, is recorded at high common inlet friction ($K_{in} = 370$), because it is clear that the large friction in the downcomer has a significant influence on the existence of inter-channel circulation, since the flow through the primary loop is in continuous competition with reverse flows in a part of the the channels.

Hysteresis

Once the system has been brought into this low subcooling stable flow regime, part of the hot coolant will be recirculated between channels. To keep it into this state, the inlet temperature does therefore not need to be as high as it was when the behavior was initiated. The same can be said for the power: less power is needed to sustain the process than to initiate it. This means that the low subcooling stable flow has, in fact, two boundaries in the power-subcooling plane: an initiation boundary and a maintenance boundary. In figure 4.9, the effect is shown schematically. Starting from the operational point at point A, which could be in the out-of-phase oscillation regime for example, we slowly decrease the inlet subcooling until the low subcooling stable flow regime is initiated at point B. This means that the initiation boundary of this regime is at point B. Now, if we decrease the inlet temperature again, the system will stay in the stable flow regime, even though less heat is added to the system. It might return to the out-of-phase regime at point A, or even at point C. This point is called the maintenance boundary, since it indicates how much energy needs to be added to the system to maintain the stable regime. The stability behavior is consequently different depending on whether we are increasing or decreasing the inlet temperature. This effect is called hysteresis. The difference between

[2] Although we are dealing with stable mass flow, the pressure drop over a channel in these conditions are high enough to calculate the partial mass flows with relatively small uncertainty (see section 3.4).

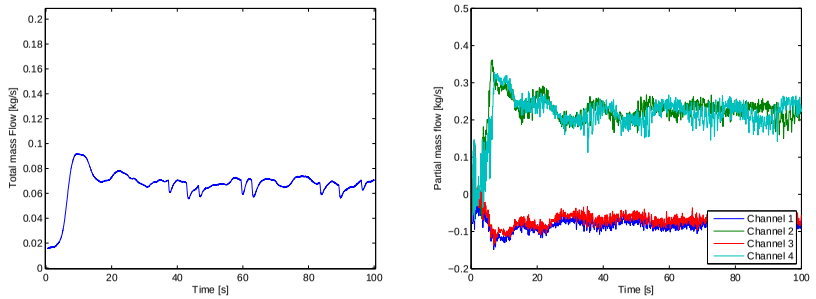

(a)

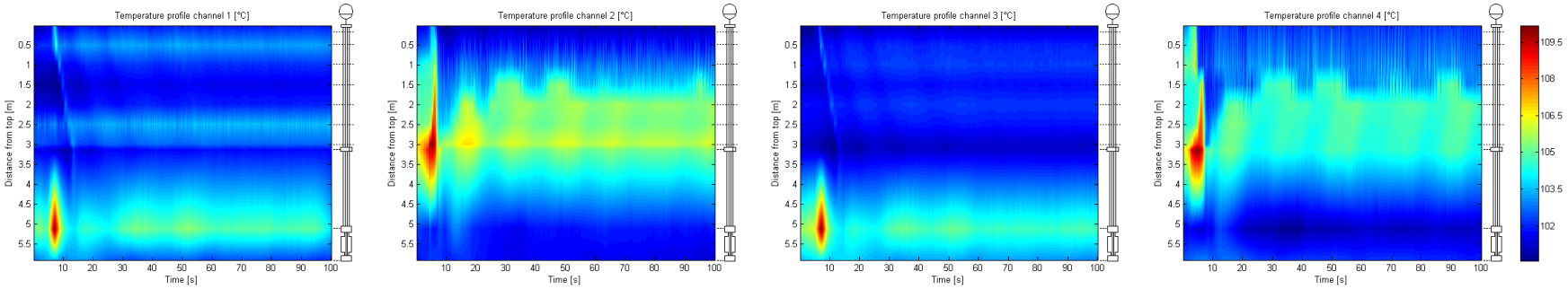

(b) Temperature profiles for each channel.

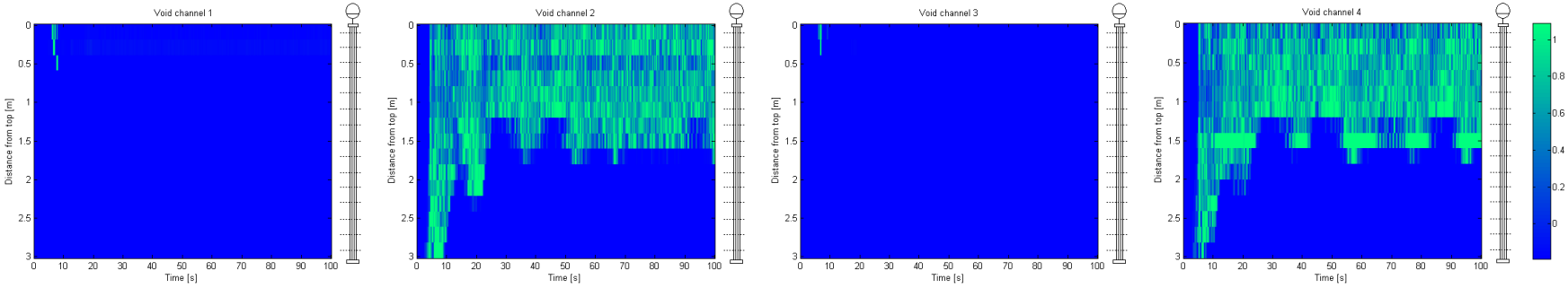

(c) Void detected in the chimney section.

Figure 4.8: The Total mass flow and the partial mass flow per channel (a), the temperature profiles (b) and void detection data (c) for low subcooling stable flow at $P = 1,8$kW, $T_{sub,exit} = 1,2$°C and $K_{in} = 370$. The time is indicated in seconds on the horizontal axes (0 - 100) and on the vertical axes the axial position of the sensor in question is given. This has been clarified by the schematic versions of the CIRCUS IV facility next to the pictures. Note that the temperature sensors are installed over the whole length of the setup, whereas the void sensors are only present in the chimney. From left to right, the images represent the channels 1 to 4, respectively.

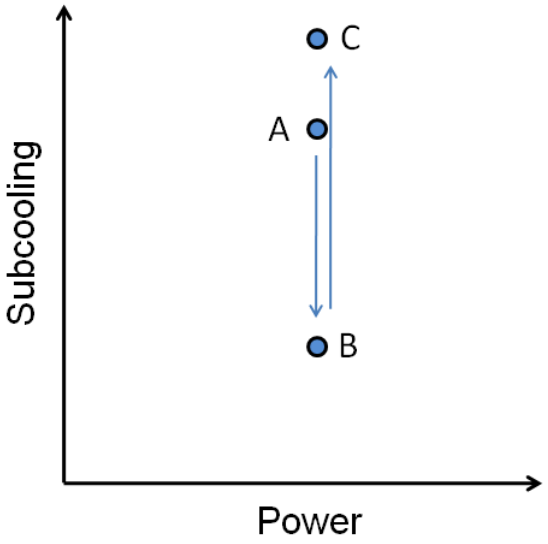

Figure 4.9: The concept of hysteresis in CIRCUS IV.

the two boundaries can be quite large and, as we will later see, a disturbance (e.g. a friction or power distribution between the channels) can be enough to attain the low subcooling stable state far below the initiation boundary.

The question might arise why no hysteresis has been found in the higher order out-of-phase flow regime. This is due to the fact that, contrary to the stable flow regime, in none of the observed oscillation states in the higher order out-of-phase regime, the inter-channel recirculation is permanent. At the moment the reverse flow stops, colder coolant will be fed to the channels from the common inlet.

At this point, we can get back to the remark made with respect to the low subcooling stable flow regime in figure 4.1. At a low common inlet friction coefficient ($K_{in} = 8,9$), this regime has been recorded, but its (initiation) boundary could not be determined. This is due to the fact that the regime was invoked by disturbing the higher order out-of-phase regime by temporarily increasing the common inlet friction in that case. After the stable flow regime was initiated, the friction was brought back to its original value. Nevertheless, the regime was maintained. Apparently, we can conclude that although the initiation boundary was not yet reached in the CIRCUS IV measurable range, the maintenance boundary was. As a result, the regime could be recorded under low common inlet friction conditions.

4.2 The stability map

The occurrence of the instabilities described in the previous section can be indicated in the power-subcooling plane. The resulting map, called a stability map, is shown in figure 4.10 for two different values for the common inlet friction

coefficient. The colored lines are second order polynomial fits for the set of highest subcooling data points of each regime. They indicate the approximate boundaries between the different regimes. In the low inlet friction stability map (figure 4.10a), five regimes can be found. Starting at high subcooling and increasing it as in figure 4.1, we pass from the stable flow regime to higher order out-of-phase oscillation states. In figure 4.10b, we encounter the same regimes, plus the low subcooling stable flow regime.

The most likely path that will be taken during the startup of a reactor, is slowly increasing the coolant temperature until enough vapor can be created to pressurize the system. As a result, the low subcooling stable regime will not be encountered until the initiation conditions are met. For this reason, the initiation boundary was chosen as the defining boundary for the low subcooling stable regime. This is the reason why this regime is not found in the low common inlet friction stability map.

One thing we notice in figure 4.10, is that the upper stability boundaries seems to pass the horizontal $T_{sub} = 0$K axis at approximately 450 W in both cases. It is expected that this is caused by the heat loss and evaporation in the channels, since, at zero subcooling, boiling would occur at the top of the chimney if no heat were lost in the system. The approximate location at which the horizontal axis is crossed, is therefore an indication of the heat loss in the core and chimney sections. This value is comparable with our estimate of the heat loss over the core in section 3.7.

4.2.1 The influence of the common inlet friction coefficient

It immediately becomes clear from the figures 4.10a and 4.10b, that the common inlet friction has a large influence on the stability of the system. At $K_{in} = 370$, the system becomes much more unstable: Instabilities are already observed at a much higher subcooling (or lower power). This effect had been expected beforehand; when the friction of the natural circulation loop was increased, a decrease of the flow through the system followed, which means that more heat can be transferred to the coolant in the core for the same inlet temperature and power conditions. It is due to the shifting stability boundaries at higher inlet friction coefficients that we have been able to study the higher order out-of-phase regime and the low subcooling stable regime in more detail.

One thing we also notice, is that the relative size of the out-of-phase regime has significantly decreased. This effect is caused by the increased reverse flow at high common inlet friction, as can be seen in figure 4.11. The data in this figure has been acquired by comparing the time averaged reverse flow to the upward flow in the channels for a large number of geysering events:

$$\text{Relative reverse flow} = \frac{\int_{t_1}^{t_2} M_{up} dt}{\int_{t_1}^{t_2} M_{reverse} dt} \tag{4.1}$$

where t_1 and t_2 mark the start and the end of the geysering event. From the information in the figure it becomes clear that at higher inlet friction coefficients, the reverse flow is relatively much higher than at low inlet friction. Due to the

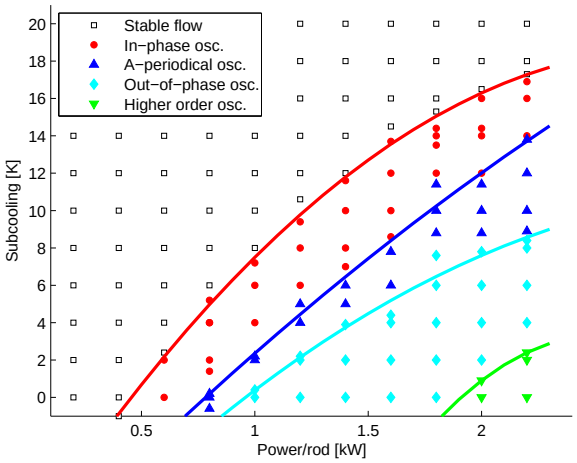

(a)

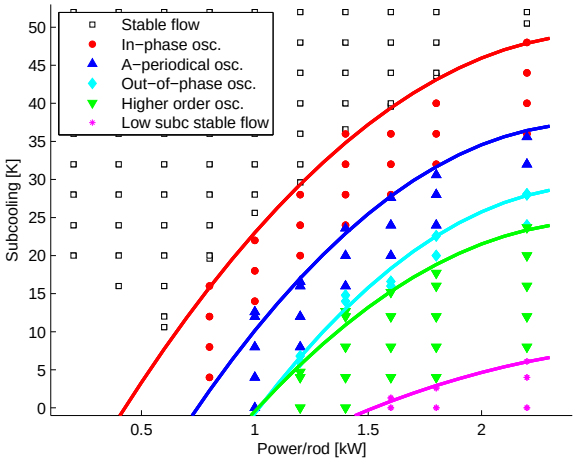

(b)

Figure 4.10: The stability maps: (In)stability behavior in the power-subcooling plane for $K_{in} = 8,9$ (a) and $K_{in} = 370$ (b). Subcooling has been taken relative to conditions at the chimney outlet. The vertical axes in these images are not at the same scale.

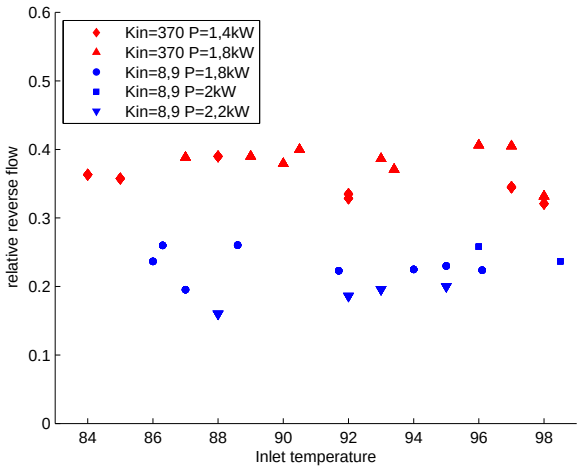

Figure 4.11: The reverse flow relative to the upward flow in geysering channels for high and low inlet frictions.

increased reverse flow, the hot coolant can already be removed from the core completely at much higher subcooling, hence giving rise to higher order out-of-phase oscillations, in which this effect plays an important role, as we have seen in section 4.1.5.

4.3 Comparison of the stability behavior of the different CIRCUS setups

One of the goals of this thesis is to study the effect of chimney division on stability. Now that we have acquired stability information on all three CIRCUS setups, we can proceed to combine the results to make some statements about chimney division.

4.3.1 Comparability

As described in chapter 3, the geometry of the CIRCUS IV setup is slightly different than its predecessors. Before we can compare the stability behavior in the different CIRCUS geometries, we will therefore study the effects of these differences on the stability of the setups and emphasize the issues that have to be taken into account during the comparison.

Chimney height

Since the chimney is approximately 50 cm taller in CIRCUS IV, it is expected that the mass flow through the facility will increase due to the additional pressure head. The resulting larger flow will give the coolant less time to heat up in

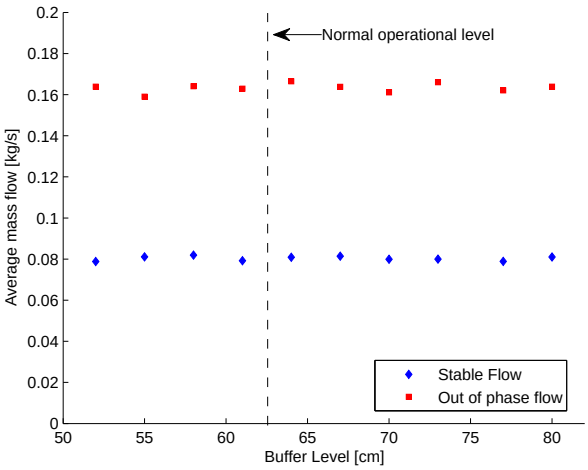

Figure 4.12: The average flow in the stable flow regimes for varying buffer level heights at $P = 1,4$kW and $K_{in} = 8,9$.

the core and therefore it is expected that CIRCUS IV will be more stable than it would be with a shorter chimney.

However, the interactions between gravitational pressure head, the heat transfer in the core and the friction in the system are not always straightforward: a smaller amount of heat transferred in the core will, in turn, have a negative effect on the thermal driving head, because of the decrease in density difference between the downcomer and the heated channels. For this reason, some experiments are conducted with a varying buffer level in CIRCUS IV. During operation in the high subcooling stable flow regime and the out-of-phase flow regime, the buffer level was decreased and increased around the standard operational level. It was found that for a fixed power and inlet temperature, a variation of the buffer level did not significantly increase the flow through the system, see figure 4.12. This is an indication that, in contrast to our expectation, the height increase of approximately 50 cm will probably not have a very large influence on the mass flow through the system.

Another effect we can expect with a taller chimney, are larger pressures in the system due to the additional static pressure. The density (and consequently the enthalpy) are nonetheless hardly dependent on the pressure in the operational range of the facility, therefore it is expected that this effect can be neglected.

Downcomer friction

Due to the decrease of the downcomer diameter (half of what it was in CIRCUS I and II, see table 3.1), the velocity of the downward flow is relatively higher. As a result, the Reynolds number will be twice as high at equal mass flow through the system. Considering that all CIRCUS setups are displaying turbulent flow in the downcomer throughout practically the whole measureable range, this will

decrease the friction coefficient in this section.[3] Nevertheless, since the total frictional pressure drop scales with the square of the velocity (see equation 3.1), the pressure drop due to friction will be higher at the same mass flow. We can conclude from this that a decrease in downcomer width will generally cause the natural circulation loop to settle at a lower flow equilibrium if the same amount of energy is added to the system. The effect on stability will be similar to the situation with a high inlet friction coefficient explained in section 4.2.1 (only much less drastic).

Inertial effects

It was found for CIRCUS I by Manera and Van der Hagen [22], that the relationship between driving pressure in the loop and kinetic pressure can be approximated by a straight line passing through the origin and that the static characteristics are well correlated regardless of whether the flow condition is stable or unstable. This means that in both stable and unstable circulation, the driving pressure and the friction are the major terms in the integrated momentum balance over the loop and that inertia does not play a major role.

It has also been found by Manera and Van der Hagen [22] and by Marcel [5], that inertia does invoke a phase lag between the void fraction in the chimney and the flow rate through the system. In the CIRCUS IV setup, the influence of inertia is not expected to differ much from the previous setups, because the total amount of coolant present in the system is approximately the same after the geometrical alterations. To test this, the cross correlation of the void detection signal and the corresponding mass flow characteristic is calculated and shown in figure 4.13. It can be seen that there is indeed a delay of approximately 0,6 s due to inertia. This corresponds well to the 0,77 s found by Marcel in CIRCUS II.

Nevertheless, this inertia effect is not expected to influence the position of the stability regimes themselves. The stability behavior is dependent on steady characteristics like the inlet temperature and the power. Although inertia may influence the flow characteristics during unstable flow, it will not determine at which conditions unstable flow occurs.

Cross-sectional area

In table 3.1 it can be seen that the total cross-sectional area of the CIRCUS IV chimneys is 8% larger in comparison to CIRCUS I. At equal mass flow, this would result in a decrease of velocity in the chimneys[4] Since the flow throughout both setups remains in the turbulent regime during single phase circulation and difference in cross-sectional area is not that large, no significant wall friction effect on the flow (and consequently the stability of the system) is expected by this small velocity increase.

[3] As can be seen in the Moody diagram. See for example [20]

[4] The core section is unchanged, so at equal mass flow, the velocity in the core and also the heat transferred to the water, remains the same.

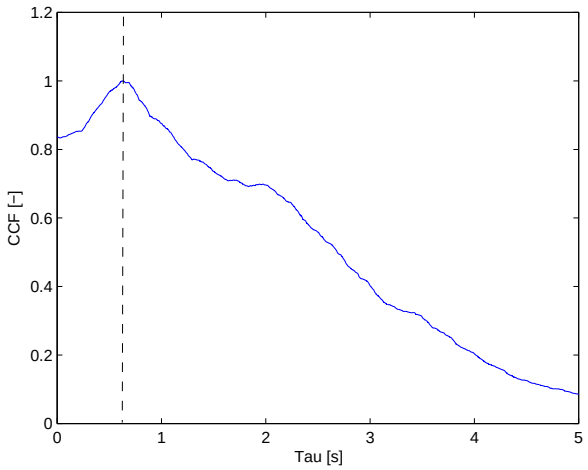

Figure 4.13: The correlation of recorded signals from the void detection (the driving force) and the corresponding mass flow in channel 1 during in-phase oscillation at $P = 1400$W and $T_{sub} = 9,5$.

4.3.2 Increase of chaotic behavior

Now that we have emphasized some of the comparability issues that have to be kept in mind, the first thing we can do, is simply compare the stability maps of the different CIRCUS setups in the power-subcooling plane in a qualitative manner. The first remark we can make is that in this plane, the CIRCUS IV setup seems to be the most stable one. [5]

Although the peripheral systems of CIRCUS I and CIRCUS II are essentially the same, the former is much more unstable as a result of the fact that measurements were conducted with a high local friction in the downcomer.[6] Extensive analysis of the data recorded by Manera [4], shows that the K-factor associated with the local frictional pressure drop is approximately $K = 128$.

Another thing we can conclude from figures 4.14a to 4.14c, is that the a-periodical regime has increased with the division of the chimney into separate parallel channels. From no reported a-periodical oscillations in CIRCUS I,[7] to an a-periodical region at high power in CIRCUS II to a large a-periodical transition zone between the in-phase and out-of-phase oscillations. Since we have seen that reverse flow plays a role in the occurrence of a-periodical oscillations, it is not surprising that the behavior was not found in CIRCUS I; it simply has no parallel channel in which a reverse flow can be induced. The question remains, however, why no a-periodical transition was found in CIRCUS II between the

[5] Be aware that we are still comparing systems with several peripheral differences, as we have just noticed in the last section. At this stage, we may not conclude that systems with four parallel channels are generally more stable than systems with two parallel channels.

[6] From personal communication with Annalisa Manera.

[7] No a-periodical oscillations were reported by Manera [4], although a study by Clausse and Lahey [23], based on a analytical, non-linear model, shows that, theoretically, a-periodical behavior could be possible in a single channel as a cascade of oscillation frequency bifurcations.

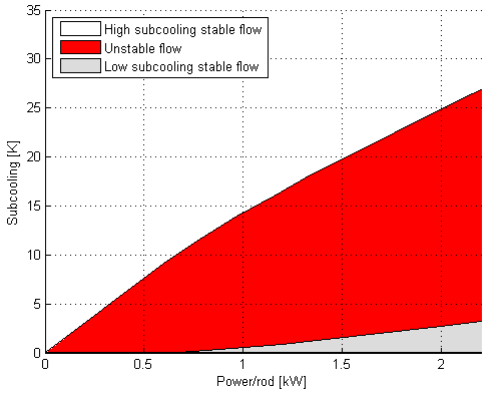

(a) CIRCUS I

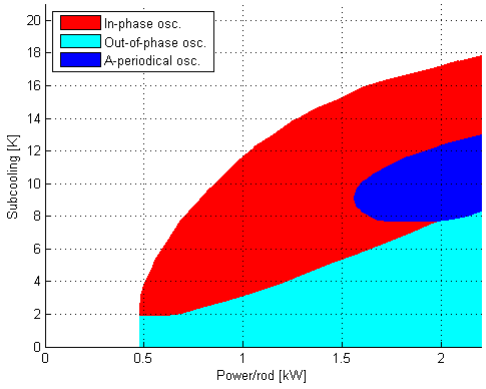

(b) CIRCUS II

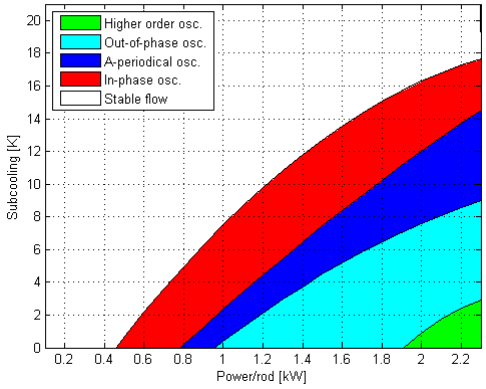

(c) CIRCUS IV

Figure 4.14: The stability maps for the different CIRCUS configurations. Sources: Manera [4], Marcel [5]. The vertical axes in the figures differ in scale. The respective stability lines have been drawn by the respective authors themselves.

in-phase and out-of-phase regions for relatively low power. It could be due to the fact that the reverse flow in these regions was very small, causing the a-periodical region in the stability map to be too small to be measured. Another possible explanation is that a-periodical oscillations were accidentally confused with out-of-phase oscillations, due to the occurrence of relatively longer intervals of periodical oscillations in these conditions.[8] More investigation into the a-periodical behavior in CIRCUS II is needed to account for this observation. Unfortunately, the measurements conducted with the CIRCUS II setup in this operational range could not be retrieved.

4.3.3 Overall stability

In the previous sections, we have compared systems in the power-subcooling plane. These are not the only parameters that play a role in the comparison of systems, however. Due to friction differences, for example, different mass flows are induced by natural circulation at the same power and inlet temperature conditions. As we have seen before, the flow also influences the stability characteristics of the system. It is therefore more logical to compare the systems in the dimensionless N_{pch}-N_{sub} plane, in which all relevant parameters are taken into account. The stability measurements from figures 4.10a and 4.10b are translated to this plane using the following relations:

$$N_{pch} = \frac{P}{Mh_{fg}} \frac{\rho_l - \rho_v}{\rho_v} \tag{4.2}$$

$$N_{sub} = \frac{h_{l,sat,ci} - h_l}{h_{fg}} \frac{\rho_l - \rho_v}{\rho_v} \tag{4.3}$$

Where P is the applied power in the core, A_c the core cross sectional area, M the (time-averaged) primary mass flow, $h_{l,sat,ci}$, h_l and h_{fg} are, respectively, the liquid saturated enthalpy at the core inlet, the liquid enthalpy at the core inlet and the specific vaporization enthalpy and ρ_l and ρ_v are the liquid and vapor density of the coolant.

In figure 4.15a the upper stability boundaries (i.e. the transitions from high-subcooling stable flow to the in-phase oscillation regime) are shown in the N_{pch}-N_{sub} plane. For easier comparison to the data presented by Marcel [5], the subcooling number has been determined with respect to the core inlet saturation enthalpy. Since CIRCUS IV is taller than its predecessors, the pressure and as a consequence the core inlet saturation enthalpy at its inlet are slightly higher. To enable comparison of the systems, the CIRCUS IV data displayed in figures 4.15a and b, has therefore been corrected for this effect, by calculating the core inlet subcooling with respect to the saturation enthalpy at the inlet of the CIRCUS II setup. Two straight lines are also shown in figure 4.15. These lines represent zero quality at the exit ($N_{pch} = N_{sub,re}$) and zero quality at the inlet ($N_{pch} = N_{sub,ci}$) of the CIRCUS II facility.

It is clear that all stability boundaries in figure 4.15a are located below the saturation line corresponding to zero quality at the chimney exit. It is expected

[8] We have discussed in section 4.1.3, that the measurement window plays a role in making a distinction between the a-periodical and the out-of-phase regimes.

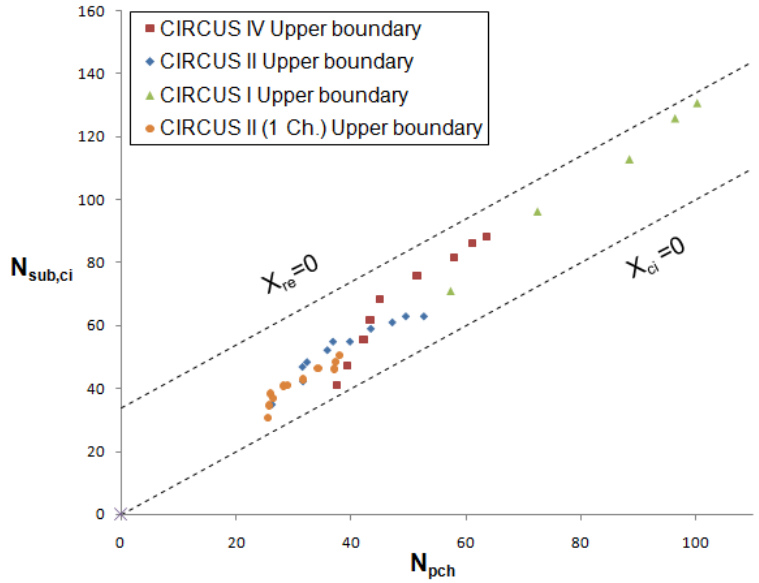

(a) The upper stability boundaries of all three CIRCUS setups and CIRCUS II operating at 1 channel for $K_{in} = 8, 9$.

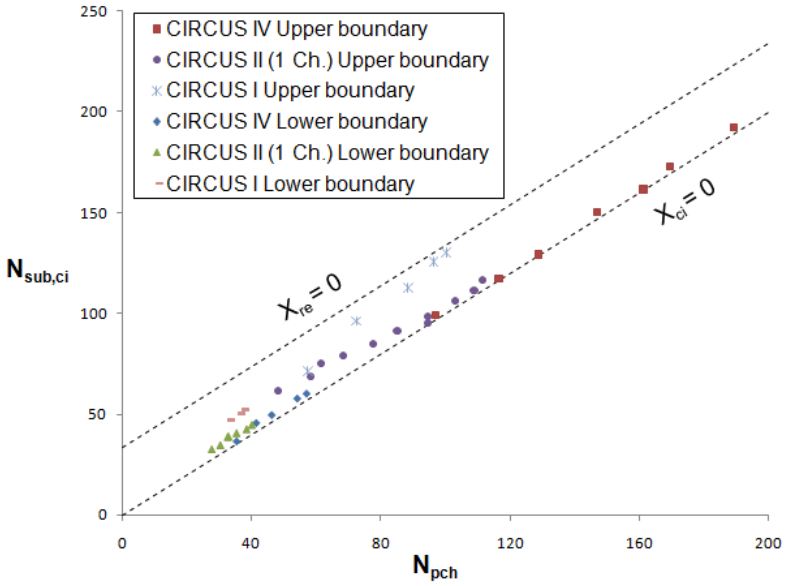

(b) The high and low subcooling stability boundaries at high inlet friction for CIRCUS II (operating at 1 channel and $K_{in} = 340$) and CIRCUS IV ($K_{in} = 370$).

Figure 4.15: Stability boundaries for the different CIRCUS configurations in the N_{pch}-N_{sub} plane.

that this effect is partly caused by heat loss from the system and partly by the production of vapor in the channels. The important implication for the ESBWR is that the reactor can be started up in the high subcooling stable natural circulation regime, while also producing vapor to pressurize the system.

Although, the data in figure 4.15a does not seem to form a neat curve, one conclusion that can be drawn from it, is that the CIRCUS IV upper stability boundary displays a shift towards the $X_{re} = 0$ line at higher subcooling numbers, with respect to the CIRCUS II stability boundaries in both the double and single channel cofiguration. This means that the high subcooling stable regime at these operational points becomes smaller and the unstable operating range becomes larger compared to the CIRCUS II setup (in both single and double channel setup). At lower subcooling numbers however, we see an opposite trend. The CIRCUS IV stability boundary is further away from the $X_{re} = 0$ line than the CIRCUS II stability boundaries. The effect could possibly be caused by an increased heat loss in CIRCUS IV at the low subcooling, and low power over flow conditions at these operational points. It must also be emphasized that the uncertainty in the determination of N_{pch} has become relatively large in this domain, due to the high relative uncertainty in the determination of the mass flow at low the corresponding low mass flow conditions. More information about the determination of the uncertainty in N_{pch} can be found in appendix C.

For CIRCUS I, a different pattern is observed. Its stability boundary is located at higher phasechange numbers, due to the increased K-factor in the downcomer and the resulting lower mass flow through the system. Due to the fact that only few data points are available and because they are spread out in the dimensionless plane, it is questionable to draw conclusions from the comparison with the CIRCUS IV and CIRCUS II stability boundaries.

When we compare figure 4.15a to figure 4.15b, we notice that a larger common inlet friction causes the stability boundaries to deviate from the chimney outlet zero quality line ($X_{re} = 0$). Also, the data is stretched out in the direction of higher phasechange numbers. The position of the upper boundaries leads us to conclude that, at the same operational point, the setup becomes mores stable when a high common inlet friction is applied. A small difference can also be noticed between the upper and lower stability boundaries of CIRCUS IV at $K_{in} = 370$ and CIRCUS II (1 Ch.) at $K_{in} = 340$. However, the two systems are too different to point out if this small shift is caused by the additional friction in CIRCUS IV, the difference in heat loss in the system, or another effect.

In addition to the location of the stability boundaries, it is interesting to investigate if the whole unstable area (i.e. the unstable area between the upper and the lower stability boundary) of the setup would widen by adding friction to the system, or if it would just display a shift in the N_{pch}-N_{sub} plane. As a reference, the CIRCUS I stability boundaries, which were observed at intermediate common inlet friction coefficient ($K = 128$), have been added to figure 4.15b. Since the low subcooling stable circulation state is only attained in high common inlet friction conditions, the only other comparison we have in this respect, are experiments conducted by Marcel [5] at the CIRCUS II setup, with one chimney closed off. No high common inlet friction measurements were conducted with the CIRCUS II double channel setup, nor was the low subcooling stable regime detected in this configuration. Comparison of the six stability boundaries in

figure 4.15b results in the conclusion that although the whole unstable regime seems to stretch out in the direction of higher phasechange numbers, the main result of adding friction to the system is a shift away from the zero quality at the chimney exit line. This means that the high subcooling stable regime is enlarged at these conditions. However, due to the fact that the low subcooling stable regime lies largely outside and at the edge of the CIRCUS measurement range, only few data points are available to base this conclusion on. Therefore, we will try a different approach in the next chapter.

Chapter 5

Simulation and verification

5.1 Theoretical model

In the introduction, the flashing phenomenon was explained and identified as the primary cause of instabilities at low pressure and low power conditions. For a flashing event to occur, the temperature of the coolant in the chimney must reach the local saturation temperature. If we assume the pressure profile over each channel to be linear, the lowest saturation temperature can be found at the top of the chimneys. When, consequently, the coolant inlet temperature is slowly increased during operation in the high subcooling stable regime, it can therefore be expected that the first flashing-induced instabilities will approximately be encountered at the moment coolant at the core exit saturation temperature reaches the top of the chimney. Using this information, it will be possible to create a simple analytical model to predict at which power and inlet temperature conditions the flashing effect is first encountered.

Just before the onset of instability, the flow would be stable. This allows for an analytical approach from the steady state perspective. Starting from the momentum balance:

$$\frac{d\rho\mathbf{u}}{dt} + \mathbf{u}\nabla\rho\mathbf{u} = -\nabla p + \rho\mathbf{g} - \mathbf{F_f} \tag{5.1}$$

where $\mathbf{F_f}$ is a model for the circumferentially averaged wall shear stress and local frictional pressure drops. It can be described by:

$$\mathbf{F_f} = \frac{1}{2}\rho K_i \mathbf{u}^2 \delta(l - l_i) + \frac{1}{2}\rho\mathbf{u}^2 \frac{f}{D} \tag{5.2}$$

where f is the friction factor related to wall friction, D the diameter of the pipes and K_i the friction coefficient for localized contributions to the pressure drop.[1] For steady state circulation, the inertia term disappears. If we integrate

[1] Although the symbol f is often used to indicate the Fanning friction factor, it is not the case here. In this thesis, the Darcy friction factor is used. The difference is a factor 4: $f = 4f_{fanning}$.

this equation over the whole closed loop, the pressure term and the convective acceleration term drop out. We are left with

$$\oint \rho \mathbf{g} dl = \oint \mathbf{F_f} dl \tag{5.3}$$

where the contour integrals are used to indicate integration over the closed loop. Working out the gravity term (the thermal driving head term), gives

$$\begin{aligned} \oint \rho \mathbf{g} dl &= \int_0^H \langle \rho_{ch} \rangle \mathbf{g} dz + \int_H^0 \langle \rho_{dc} \rangle \mathbf{g} dz \\ &= \langle \rho_{ch} \rangle \mathbf{g} H - \langle \rho_{dc} \rangle \mathbf{g} H = \Delta \rho \mathbf{g} H \end{aligned} \tag{5.4}$$

Where H is the height of the facility, $\langle \rho_{ch} \rangle$ the average density of the coolant in the heated channel and $\langle \rho_{dc} \rangle$ the average density of the coolant in the downcomer channel. Since the setup consists of sections of different geometries, we can split up the frictional pressure drop term into several components, one for each section:

$$\begin{aligned} \Delta p &= \Delta p_1 + \Delta p_2 + ... + \Delta p_n \\ &= \sum_{i=1}^{n} \frac{1}{2} \rho_i K_i u_i^2 + \sum_{j=1}^{n} \frac{1}{2} f_j \frac{(u_j)^2}{D_j} \rho_j l_j \\ &= \frac{1}{2} \sum_{i=1}^{n} \rho_i \left(K_i + f_i \frac{l_i}{D_i} \right) u_i^2 \end{aligned} \tag{5.5}$$

Where, in the last term, all the localized frictional pressure drops in each section have been combined. Combined, the two terms in equation (5.3) provide us with the following relation:

$$\Delta \rho g H = \frac{1}{2} \sum_{i=1}^{n} \rho_i \left(K_i + f_i \frac{l_i}{D_i} \right) u_i^2 \tag{5.6}$$

Secondly, we can compose an energy balance for the steady state situation. For this we assume that the heat flux from the electrically heated rods in the core is constant and axially uniform. We also neglect variations in the inlet subcooling and enthalpy variations with pressure. If we assume that all power applied to the heating rods is absorbed by the coolant, the energy balance simply becomes:

$$\Delta h = \frac{q}{M} = \frac{q}{\rho_c u_c A_c} \tag{5.7}$$

where $\Delta h = h_{c,out} - h_{c,in}$ is the enthalpy change in the core, q the applied core power and M the mass flow through the system. ρ_c, u_c and A_c are respectively the density, coolant velocity and cross-sectional surface area in the core. We have seen that there is a significant heat loss from the channels. Equation 5.7 therefore becomes:

$$\Delta h = \frac{(q + q_{loss})}{\rho_c u_c A_c} \tag{5.8}$$

Where q_{loss} is introduced as the heat loss.

Making use of the equations (5.6) and (5.7), a stability boundary can be calculated. From a given h_{in} (T_{in}) and the fact that the enthalpy of the coolant exiting the core must be equal to the saturation enthalpy at the top of the chimneys ($h_{sat,re}$), we can calculate Δh. Using equation (5.7), we have established a relation between h_{in} and the applied power necessary to initiate flashing at this inlet enthalpy, q: Exactly the information we would need to draw the stability line in the power-subcooling plane. After a value for u_c is obtained through equation (5.6), q can be calculated. The relation for the stability boundary becomes:

$$q = \frac{h_{sat,re} - h_{in}}{\rho_c A_c} \sqrt{\frac{\frac{1}{2}\sum_{i=1}^{n} \rho \left(K_i + f_i \frac{l_i}{D_i} \right)}{\Delta \rho g H}} - q_{loss} \tag{5.9}$$

For the calculation of the coolant density throughout the system, the XSteam Matlab package is implemented. We see from equation (5.9), that to be able to calculate the stability boundary, expressions for the friction coefficients in the system must be known, which is the subject of the next section.

As we are modeling a single phase, steady state system, there is no reason why we could not extend the single channel situation to multiple parallel channels, as long as we adjust for the additional wall friction due to channel division.

5.2 Friction

The calculation of the friction in the setup is one of the most important parts of the model. We can experimentally determine the K-factors, that are related to the concentrated frictional pressure drops of valves, bends, inlets etc., over the parts of the setup where differential pressure sensors are present. This can be done, for example, at the chimney exit, the core inlet channels and the common inlet friction valve (see figure 3.2). The other friction factors will have to be evaluated by means of standard geometry-based correlations.[2] An overview of the measured and calculated K-factors can be found in table 5.1, the descriptions refer to the schematic of CIRCUS IV in figure 3.2.

For the wall friction coefficients, expressions are available in the literature.[3] At laminar flow conditions, the Darcy friction factor is given by:

$$f = \frac{64}{Re} \tag{5.10}$$

and in turbulent conditions, an approximation of the friction factor for a full flowing circular pipe was given by Haaland [24]:

$$\frac{1}{\sqrt{f}} = -1,8 log_{10} \left[\left(\frac{\varepsilon/D}{3,7} \right)^{1,11} + \frac{6,9}{Re} \right] \tag{5.11}$$

[2] See for example Dekkers and Wijnen [26] or Idelchik [27].
[3] See for example Todreas and Kazimi[28].

Section	K-factor
Common inlet valve	8,9
Channel inlet (valves & bends)	3,45
Chimney outlet	1,7
Pre-heater vessel	0,7
Buffer vessel	0,4
Expansion vessel	1,2
Left bottom bend	0,15
Total	16,5

Table 5.1: Measured and calculated friction coefficients in the CIRCUS IV setup.

A convenient relationship that incorporates both the laminar and turbulent flow regimes with a transition to turbulent flow at $Re = 2100$ is that of Churchill:[4]

$$f = 8\left[\left(\frac{8}{Re}\right)^{\frac{1}{12}} + (a+b)^{-\frac{3}{2}}\right]^{\frac{1}{12}} \tag{5.12}$$

With:

$$\begin{aligned} a &= \left[2,457ln\left(\left(\frac{7}{Re}\right)^{0,9} + 0,27\frac{\varepsilon}{D}\right)\right]^{16} \\ b &= \left(\frac{37530}{Re}\right)^{16} \end{aligned} \tag{5.13}$$

Notice that, since the wall friction coefficient depends on the flow velocity (the Reynolds number), we will have to conduct an iteration with equations (5.6) and (5.12), to find the velocity in the system.

5.3 Modeling of the out-of-phase and a-periodical stability boundaries

The prediction of the upper (in-phase) stability boundary is not the only one that can be predicted by the simple model discussed in section 5.1. While studying the instability phenomena in chapter 4, we noticed that one of the defining characteristics of the unstable regimes in the stability map is the location of vapor production. In-phase flow oscillations are driven by flashing, whereas out-of-phase oscillations are caused by geysering. During a-periodical oscillations both phenomena play a role.

Another way to formulate this conclusion for the out-of-phase regime specifically, is that an out-of-phase situation can only be sustained indefinitely if geysering can always occur. This is an observation we can easily turn into a requirement similar to that for the upper stability boundary, by setting the enthalpy of the

[4]See for example Oliemans [25].

coolant leaving the core equal to the saturation enthalpy at the core exit. By using the described model, we apply the simplification that geysering occurs in steady state conditions. This is a simplification of reality, but admissible since we are only trying to calculate at which power and inlet temperature conditions, geysering *must* happen, not when it occurs in dynamic conditions.

For the a-periodical regime, things are a little more complicated. We have seen that the defining characteristic for the occurrence of a-periodical behavior is reverse flow. As long as a large enough reverse flow is induced during geysering or flashing events, a cascade of geysering events can be sustained indefinitely. In practice, however, this cascade will sooner or later "miss a step" due to a certain perturbation and leave room for a flashing event. The reverse flow can be experimentally determined in CIRCUS IV (see for example figure 4.11), but it has at the same time shown to be highly dependent of the application of local friction coefficients in ways that are not yet quantitatively described. Additionally, to allow extension of the model to different geometries and multiple channels, a general relation that predicts the reverse flow in all situations has to be found first, avoiding reliance on experimentally determined relations. At this point, therefore, the boundary of the a-periodical regime cannot be predicted by analytical means.

5.4 Results

Using the relations presented in section 5.2 to model the friction in the system and assuming a constant heat loss of 450W per channel, the model is implemented in the Matlab environment. In figure 5.1, the simulated stability boundaries are displayed against the measured stability map. For the low inlet friction case, both predicted boundaries coincide with the measured ones quite well. We can conclude that the assumptions were correct: The in-phase oscillation is first encountered when the coolant reaches the saturation temperature at the top of the chimney and the boundary between the a-periodical and the out-of-phase oscillations are governed by achieving a geysering state at zero reverse flow.

For the high inlet friction case, the predicted in-phase stability boundary also corresponds quite well with the experimental data. The out-of-phase boundary, however, is in the middle of the a-periodical region. The deviation from the measurements is due to the fact that geysering/reverse flow-induced a-periodical oscillations extend the a-periodical regime into the out-of-phase regime in this case. As we have already seen in section 4.1.3, this type of a-periodical behavior has previously been observed at high inlet friction conditions. Further investigation of the experimental data around the predicted out-of-phase stability boundary, shows that it indeed marks the transition from flashing/geysering-induced a-periodical oscillations to geysering/reverse flow-induced a-periodical oscillations. From this we can conclude that although the predicted boundary does not correspond with the boundary of the out-of-phase regime anymore, it still correctly predicts the point at which geysering must occur.

Nevertheless, we must conclude that the condition that geysering must always occur is not enough to guarantee out-of-phase oscillation at high inlet friction.

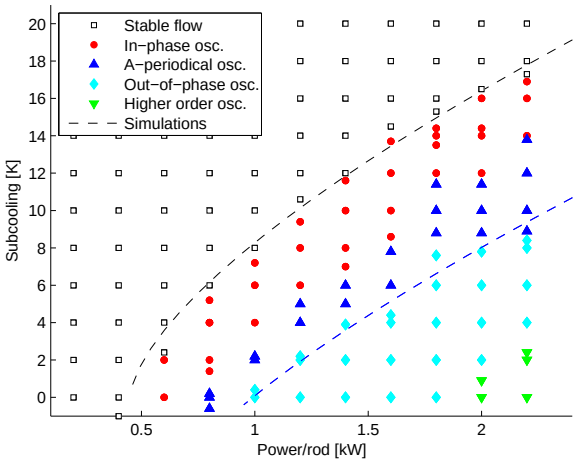

(a) $K_{in} = 8, 9$

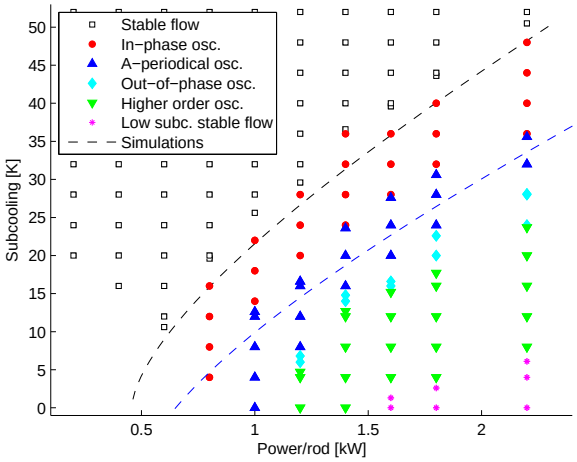

(b) $K_{in} = 370$

Figure 5.1: The experimentally determined stability map for CIRCUS IV and the prediction of the upper stability boundary and the out-of-phase oscillation boundary for a common inlet friction of (a) $K_{in} = 8, 9$ and (b) $K_{in} = 370$.

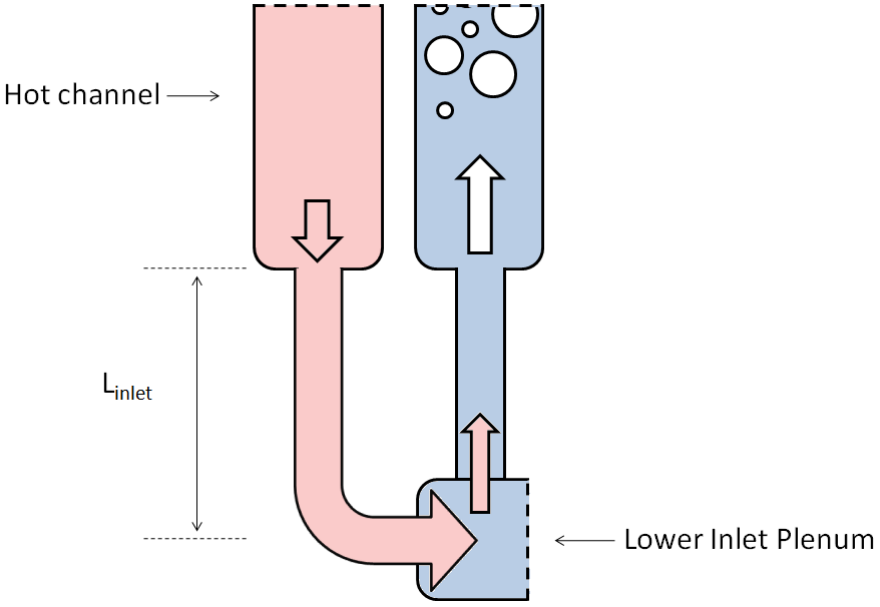

Figure 5.2: A schematic of two of the inlet channels between the core and the lower inlet plenum.

The correct transition to the out-of-phase regime can only be predicted once a relation for the magnitude of the reverse flow has been found. For now, we will treat this discrepancy as a boundary condition to the model. We have seen in section 4.1.3, that the out-of-phase regime is disturbed at the moment the reverse flow becomes large enough to pass through the lower inlet plenum and feed hot coolant to the other channels. This is illustrated schematically in figure 5.2. We can therefore expect the model to be correct if the distance covered by the reverse flow, is smaller than the distance from the core of a channel to the lower inlet plenum. The condition becomes:

$$\frac{\int_{t_1}^{t_2} v_{rf} dt}{L_{inlet}} = \frac{L_{rf}}{L_{inlet}} \leq 1 \tag{5.14}$$

Where v_{rf} is the reverse flow speed in the channel and t_1 and t_2 the start and the end of the reverse flow. L_{inlet} is the length of the inlet channel between the lower inlet plenum and the core inlet, as indicated in figure 5.2.

In figure 5.3a, the modeled and experimentally determined stability boundaries for the in-phase and out-of-phase oscillations in CIRCUS IV are plotted in the dimensionless N_{pch}-N_{sub} plane. For the in-phase stability boundary, the experiments at higher phase change numbers seem to correspond well to the predicted values, but at lower values, the experiments deviate from the model. Due to the high relative uncertainty in the determination of the flow through the system at low mass flows, it is hard to draw a conclusion from this information. Error

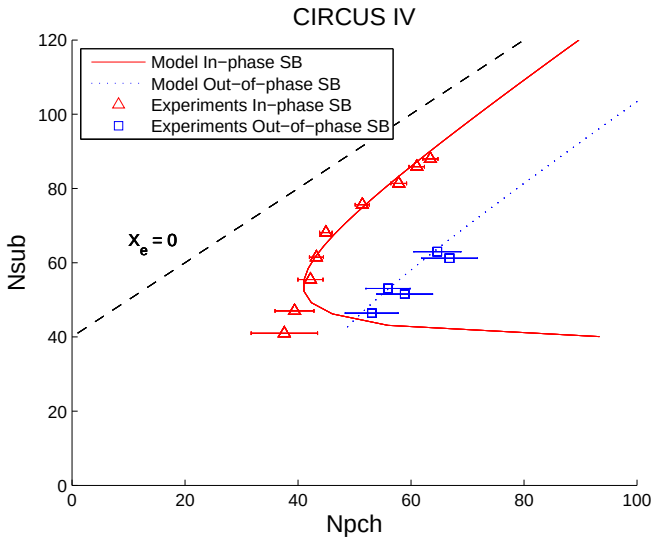

(a)

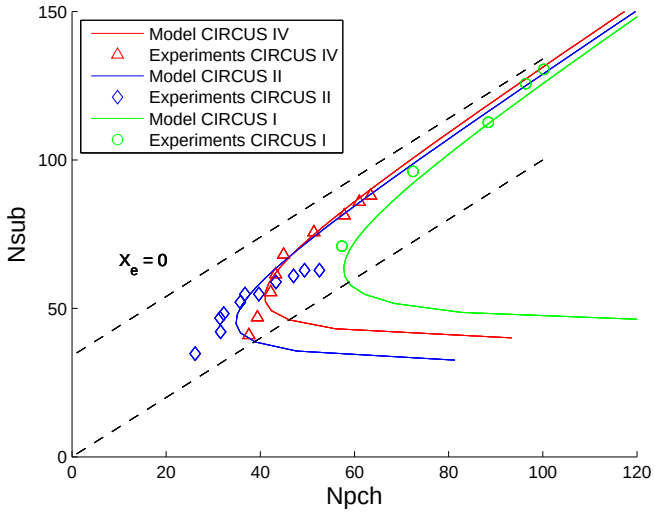

(b)

Figure 5.3: The predicted and measured stability in-phase and out-of-phase stability boundaries for the CIRCUS IV setup (a) and the in-phase stability boundaries for CIRCUS I - IV compared to experiments conducted by Manera [4] and Marcel [5].

bars have been added to show the extent of the uncertainty in the phase change number due to the uncertainty in the determination of the flow. Nevertheless, it seems that there is some effect at low mass flows that the model fails to predict. One effect that plays a role in these conditions, for example, is the additional driving head introduced by extracting heat from the coolant at the top of the facility. The effect is negligible during normal operation, but it is shown to be able to drive a very small flow through the system when no power is applied to the heating rods. It is believed by the author that this effect plays a large role in the deviation from the predicted stability boundary.

For the determination of the phase change number for the out-of-phase stability boundary data, the time-averaged minimum value for the primary mass flow is used, since the geysering oscillations are occurring from a steady single phase flow circulation in each channel. Due to the strong fluctuation of the minimum mass flow, the uncertainty in the determination of N_{pch} is quite large (indicated by error bars in figure 5.3a). As with the upper stability boundary, the experimental data corresponds well to the predicted out-of-phase stability boundary.

Moreover, the predicted values for the in-phase stability boundaries of the previous CIRCUS configurations also correspond well to the experiments, as can be seen in figure 5.3b. The experimental data from the CIRCUS I setup is shifted towards the right due to the relatively high power over flow as a result of the high common friction coefficient applied during measurements, but the model predicts this behavior correctly. We can conclude from the results in figures 5.1 and 5.3, that the driving head and the frictional pressure drop are indeed the terms that are most important for stability in the system and that the constant heat loss approximation is acceptable. The model approximates the stability boundaries for the in-phase and out-of phase regimes well enough to allow for extension to systems with larger numbers of parallel channels.

5.5 Extension to n channels

Now that we have verified the model against experimental data acquired over the past years, we can continue to extend the model to geometries with more parallel channels. For this extension of the model, we will keep all parameters related to the geometry of the setup (e.g. the localized frictional pressure drops and the diameter of the downcomer) the same as in the CIRCUS IV setup.

In figure 5.4a the in-phase stability boundary is extended to a system with 8, 16 and 64 channels. From the trends in the figure it can be concluded that the division into many separate channels has a destabilizing effect on the in-phase stability boundary for a system operating at a fixed power. In-phase mass flow oscillations are already encountered at a much higher subcooling. In fact, the stability boundary seems to be quite sensitive to channel division. Since the peripheral geometry was kept the same during all simulations, it must be concluded that the increased instability is due to wall friction added by channel division.

In the dimensionless N_{pch}-N_{sub} plane, division of the core and chimney sections into separate channels, causes the in-phase stability boundary to shift to the

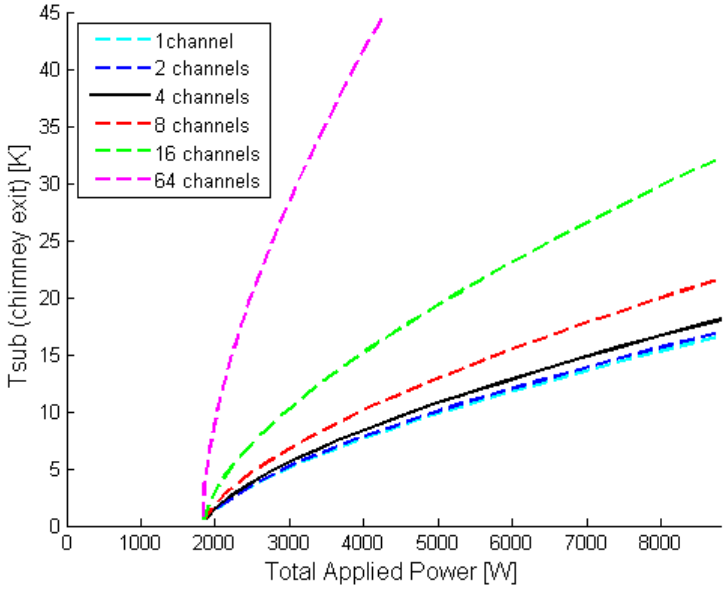

(a) The predicted in-phase stability boundaries in the power-subcooling plane for multiple parallel channels in the CIRCUS IV geometry.

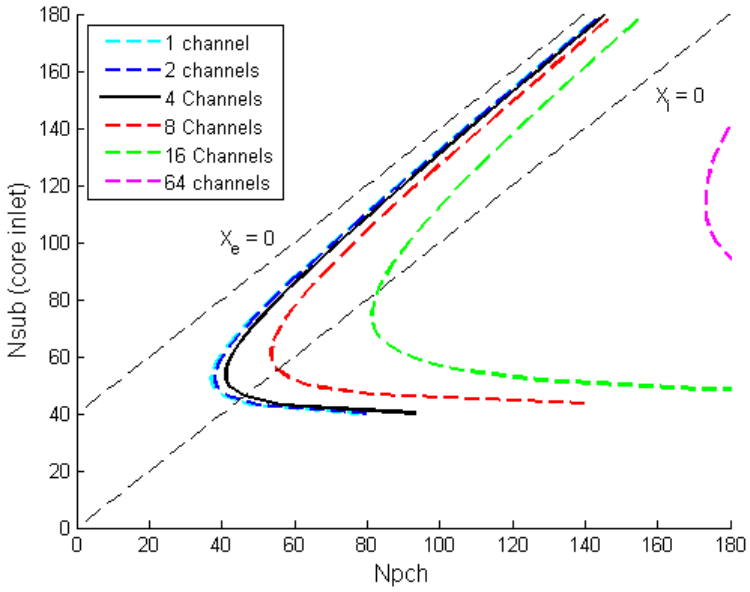

(b) The predicted in-phase stability boundaries in the dimensionless N_{pch}-N_{sub} plane for division of the core and chimney cross-sectional area into n channels.

Figure 5.4

right, as can be seen in figure 5.4b. This is in accordance with the trends displayed in the power-subcooling plane. For example, suppose we supply an equal, fixed power and inlet temperature to two natural circulating systems that are identical in any way except for the measure of channel division. The core and chimney of system A is partitioned into eight separate channels, whereas system B is fitted with sixteen parallel channels. The operational point of these facilities has been indicated in figure 5.4a. It can be noticed from the system that system A is stable at the indicated operational point and system B is unstable, since it is located below the predicted stability boundary for division in sixteen channels. Due to less wall friction in system A, the induced mass flow through the system will be larger in that system. As a consequence, the operational point of system A in the dimensionless plane will shift to the left with respect to the operational point of system B, due to the inverse dependence of N_{pch} on the flow. This shift is indicated in figure 5.4b. We see that the predicted stability of the systems at the indicated operational points has not changed. This means that both results support the same conclusion: Division into separate channels has a destabilizing effect on the system. In this plane, it can also be noted that the unstable behavior increases quite rapidly with the number of separate channels into which the core and chimney are divided: The 64 channel in-phase stability boundary has significantly shifted to the right5.4b.

The trend of stability boundaries shifting towards the right and away from the chimney exit zero quality line in the dimensionless plane is also in concurrence with the trend found in chapter 4 during the comparison of systems with an increasing common inlet friction coefficient (figure 4.15b). This accordance was expected, since the model predicts the stability boundary from a single phase, steady state situation. As a result, the location and origin (i.e. wall friction or local friction) of the friction in the system does not influence the location of the stability boundary.

Since the model was also shown to apply for the out-of-phase boundary, we can expect a similar shift towards the right of the dimensionless plane in combination with a diversion from the $X_e = 0$ line. In figures 5.5, both the in-phase and out-of phase stability boundaries have been plotted for different levels of channel division. Bear in mind that although the results in the dimensionless plane should be applicable to all systems at the same operational point, condition 5.14 has to be met for a correct prediction of the out-of-phase stability boundary. If not, this means that a prediction was only made for the boundary below which only geysering events will be encountered. The actual behavior of the system will in that case most likely be a-periodical, as discussed in section 5.4.

From the figures it can be concluded that the out-of-phase stability boundary indeed shows a similar trend as the in-phase stability boundary. Also, the out-of-phase boundary stays below the in-phase stability boundary in the CIRCUS IV operational range, which means that at increasing the inlet temperature from a stable circulation, in-phase oscillations will always be encountered before the oscillations become a-periodical. We can therefore conclude that for systems at the same operational point in the N_{pch}-N_{sub} plane, the system with largest chimney division will be most stable with respect to both in-phase and out-of-phase behavior.

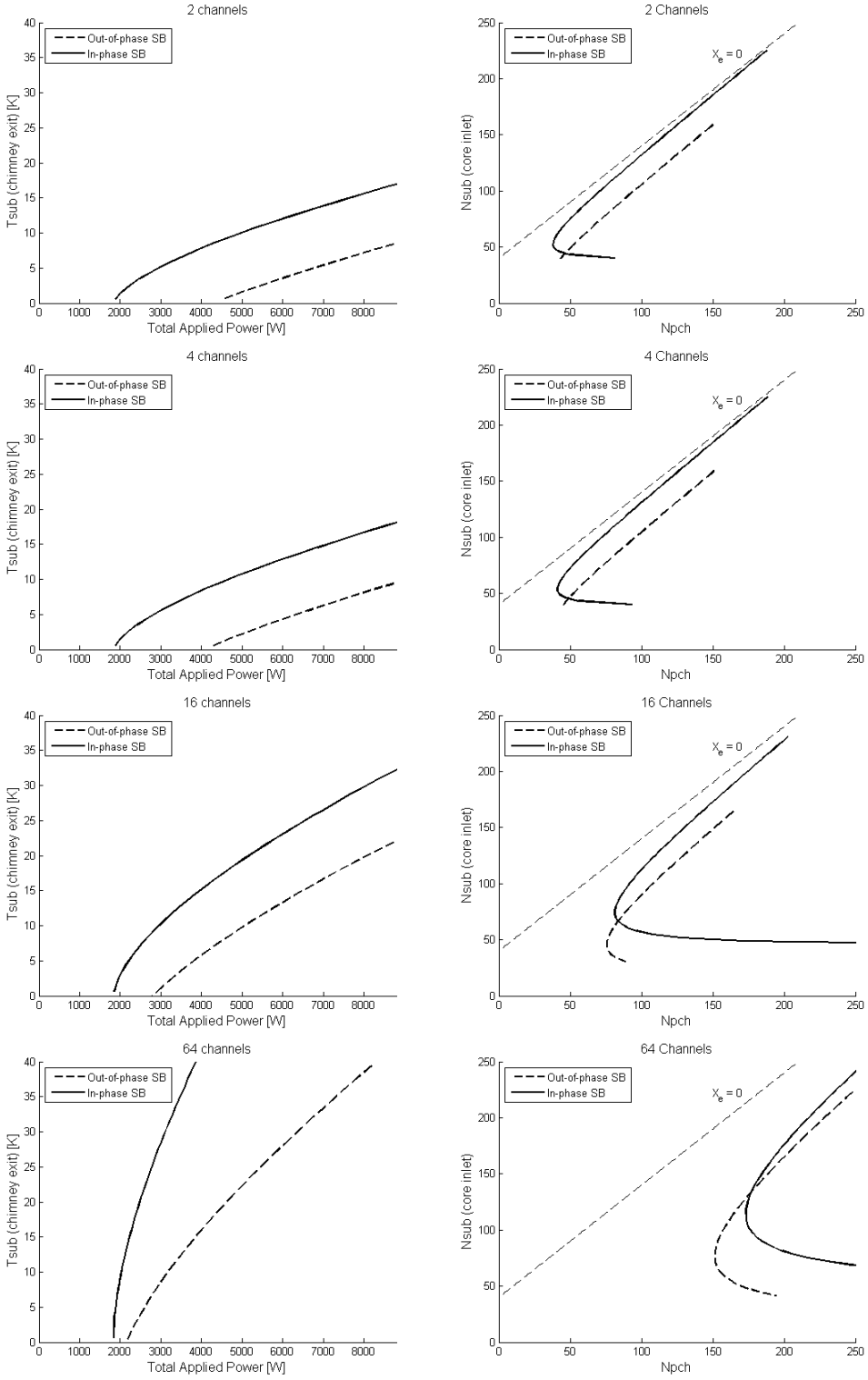

Figure 5.5: An overview of the in-phase and out-of-phase stability boundaries (SB) for different measures of channel division.

Chapter 6

Parameter study

In the previous chapters we have studied the stability behavior in systems with parallel channels. We must however not forget, that we are still dealing with a nuclear reactor. Some of the boundary conditions that have been used while studying the stability behavior of the multi-channel systems might not be realistic in a real reactor. One of these is the power profile. So far, we have assumed that power is applied to each channel equally. In the ESBWR, or any other Boiling Water Reactor, such a flat power profile is not realistic due to the geometry of the reactor. This means that the applied power will depend on the location in the reactor. The effects of such a power skew on the stability of the parallel channel natural circulation BWR is the topic of the first part of this chapter. In the second part of the chapter, a proposed method to compensate for the effects of a power skew by applying localized friction to the inlets of the separate channels is investigated. Finally, in the last section of this chapter, the implications of the acquired results to ESBWR stability will be discussed.

6.1 Power skew

To simulate the effects of a power skew in the CIRCUS facility, a 10% and 20% higher power (P_{top}) is applied to one of the heated channels with respect to the other three (P_{low}). The average power per rod applied to the system can therefore be designated $P_{avg} = \frac{1}{4}P_{top} + \frac{3}{4}P_{low}$. Friction coefficients and all other parameters are kept at the same values as during the low inlet friction stability experiments in chapter 4.

6.1.1 Stability effects

We can see in figures 6.1a and 6.1b that imposing a power skew has a significant effect on the occurrence of the different instability phenomena in the setup. The size and arrangement of the instability regimes in the power-subcooling plane deviates from the equal-power situation displayed in figure 4.10a (indicated by the dashed lines in figures 6.1) and continue to change with increasing power

skew. The most interesting observation, is that the position of the upper stability boundary moves upward in the power-subcooling plane. This means the facility as a whole becomes less stable at the same applied power.

The increased instability can be explained by the fact that, as we have claimed in chapter 5, the setup first becomes unstable at the moment the coolant reaches the saturation temperature at the top of the chimney. Theoretically, the channel operating at P_{top} will reach this point at higher subcooling than a system with four channels all equally operating at P_{avg}. The fact that three other channels in the power skew have not become unstable yet, does not change the fact that the facility as a whole displays unstable behavior, hence the upward movement of the stability boundary in the power-subcooling plane.

The effect of the power skew becomes even more interesting when we compare the upper stability boundary in another way. In figure 6.2 the measured stability boundary at a flat power profile is indicated by the dashed line. Subsequently, the upper stability boundary at 20% power skew is compared to this line in two different ways. The red line indicates the stability line determined on the basis of P_{avg}, as was done in figure 6.1. The blue line, however, indicates the same stability line determined on the basis of P_{top}. Comparing the flat power profile and 20% power skew situation in the latter way, means that we are comparing the stability boundary of the power skew to the stability boundary of a flat power profile in which P_{top} is applied to *each* rod.

From figure 6.2, we can conclude that the upper stability boundary during a power skew in which the maximum power is P_{top}, does not deviate much from that of a flat power profile that is completely at P_{top}. We can therefore conclude that the stability of the system as a whole is approximately governed by the channel to which the highest power is applied. This is an interesting result for multi-channel natural circulation reactors. The small increase in stability we do notice in figure 6.2, is thought to be due to the fact the the four chimneys are combined into a single channel at the top of the chimney. This means some mixing will occur between the relatively hot coolant from the high-power channel and the colder coolant from the other channels, causing the power skew situation to be slightly more stable than the reference flat power profile at P_{top}.

Since the mass flow has not significantly changed during the application of the power skew, we see the same trends in the dimensionless plane. This is shown in appendix D.

6.1.2 Shifting stability regimes

In addition to the deviation of the upper stability boundary, the location of the instability regimes in the power-subcooling plane differs significantly. In figures 6.1a and 6.1b, it can immediately be seen that the in-phase oscillation regime becomes larger at increasing power skew, not only due to the upward shift of the upper stability boundary, but also by extending downward in the power-subcooling plane. Apparently, in-phase oscillations are sustained for a larger range of power and inlet temperature conditions. It is expected that this is due to the fact that the reverse flow in channel 1, induced by geysering events in channels 1-3, is smaller. This is shown schematically in table 6.1. As a

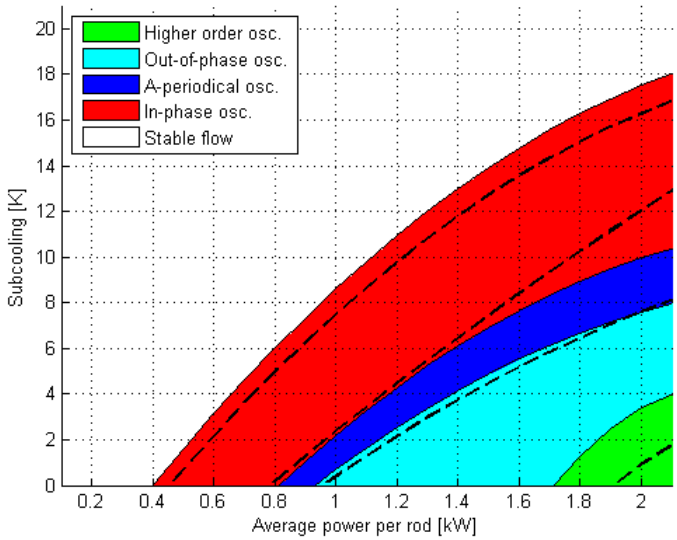

(a)

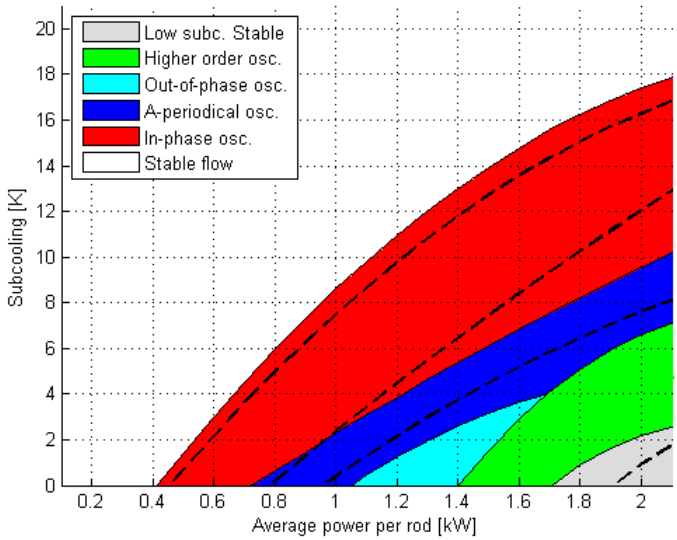

(b)

Figure 6.1: The stability map for a situation with a 10% higher power (a) and a 20% higher power (b) in channel 1 as a function of P_{avg}. The dashed lines indicated in the figure represent the stability boundaries for a flat power profile.

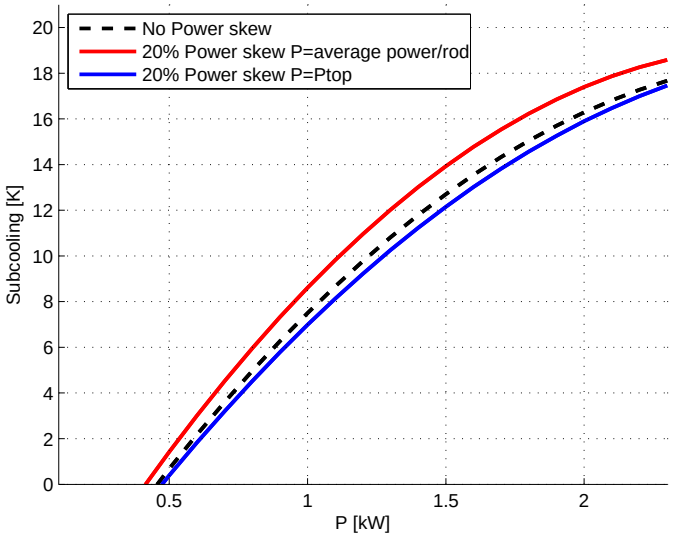

Figure 6.2: The in-phase stability boundary for a flat power profile compared to the in-phase stability boundary in a 20% power skew situation. For the same measurement, the power skew stability boundary is displayed as a function of P_{top} and as a function of P_{avg}.

	t_1	t_2	t_3	t_4
Ch.1	F	↓	F	↓
Ch.2	↓	G	↓	G
Ch.3	↓	G	↓	G
Ch.4	↓	G	↓	G

Table 6.1: In-phase oscillation during a power skew: The induced reverse flow in channel 1 is smaller than would be the case with a flat power profile at equal total power. The intervals between the events are not constant.

consequence, it takes a lower subcooling to induce a secondary geysering event in channel 1. This way, the cascade of geysering events leading to a-periodical behavior is prevented.

We also notice that the a-periodical regime is moving downwards with increasing power skew. The a-periodical oscillations at low subcooling were found to be similar to those described as geysering/reverse flow-induced a-periodical oscillations in section 4.1.3. It is found that the average reverse flow in the low-power channels is higher than in the channel operating at P_{top} and also higher than the reverse flow in a flat power profile at P_{avg}. As a result, hot coolant can be brought into the lower inlet plenum, facilitating the occurrence of this type of a-periodical behavior. At high power, the reverse flow even becomes so dominant that the out-of-phase regime is not encountered at all: the a-periodical regime borders the higher order out-of-phase regime.

The upward shift of the higher order out-of-phase regime itself is interesting too.

We have seen in chapter 4, that these oscillations are driven by geysering and reverse flow. In addition, the oscillations are usually asymmetrical in the sense that only reverse flow is encountered in some channels, whereas only geysering is encountered in the other channels. The combination of the increased reverse flow in the low-power channels and the asymmetry of the power skew, can therefore be expected to facilitate higher order out-of-phase oscillations at much higher subcooling.

Even more interesting, is that the low subcooling stable flow regime is encountered in the 20% power skew situation. Apparently, the low subcooling stability boundary moves upwards considerably. Considering that the upper stability boundary has not moved that much in the power-subcooling plane, the total unstable regime between the two boundaries is significantly decreased. In chapter 4, we already noticed that there were, in fact, two different stability boundaries associated with low subcooling stable flow: an initiation boundary and a maintenance boundary. The detection of the low subcooling stable regime in a power skew situation can be explained by the fact that the initiation of the inter-channel circulation associated with low subcooling stable flow, can occur at much higher subcooling. This is made clear in figure 6.3. Starting from point A, where the system is in the higher order out-of-phase regime, we slowly decrease the inlet subcooling. At point C, we would encounter the low subcooling stable flow in a setup with a flat power profile. Point C is therefore called the initiation boundary. At this point, the coolant would start to partly recirculate between channels, as explained in section 4.1.6. If we increase the subcooling again, the system returns to the higher order out-of-phase regime in point D, which is therefore called the maintenance boundary. Due to the application of a power skew and the resulting asymmetry between the channels, the inter-channel recirculation, and therefore the low subcooling stable regime, is already initiated at point B. If we subsequently reduce the inlet temperature again, the low subcooling stable regime can again only be maintained until we arrive at point D.

We can conclude from this that by applying a power skew, the separation between the initiation boundary and the maintenance boundary in the power-subcooling plane is decreased. It is expected that this effect becomes even stronger for larger power skews, since these would increase the asymmetry of the induced reverse flow in the system. For multi-channel systems in which power skews are encountered, this means that it is useful to investigate the exact location of the maintenance boundary in the power-subcooling plane, since it determines when the regime can occur in contrast to the initiation boundary, which only indicates when it must occur.

6.1.3 Time dependent behavior

All instabilities encountered during power skew measurements can be clearly classified into one of the six regimes described in chapter 4, with one notable exception. When the system first becomes unstable at high subcooling, we encounter a previously unobserved type of oscillation. In figure 6.4, the total and partial mass flow characteristics of such an instability is shown. We see that, logically, the high-power channel (channel 1) shows a flashing-induced instability

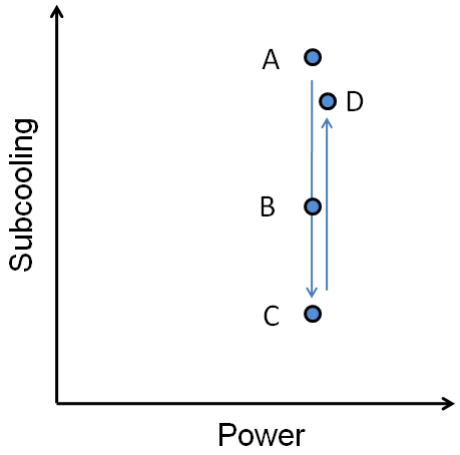

Figure 6.3: A schematic representation of the different boundaries involved with low subcooling stable flow. Point D is moved somewhat to the right for clarity; in the example the power is the same for all points.

	t_1	t_2	t_3
Ch.1	F	↓	↓
Ch.2	↓	F	↓
Ch.3	↓	↓	G
Ch.4	↓	↓	G

Table 6.2: Flashing induced oscillation at conditions just below the stability boundary in the power-subcooling plane (at $P_{top} = 2,2$ kW (channel 1), $P_{low} = 2,0$kW and $T_{sub} = 17,3$K). t_1 and t_2 are separated in time by approximately 20 seconds, t_3 follows t_2 within seconds.

first. After that, nothing happens for almost 20 s, before the other three channels display in-phase oscillation. The interesting thing is that even at power and inlet temperature conditions just below the stability boundary, flashing events do not only occur in the high-power channel. Apparently, flashing induced instabilities also occur in the low-power channels, at conditions in which they would not occur in a flat power profile. It is believed that this is due to a slightly lower mass flow in the low-power channels, but this cannot be experimentally verified due to the high relative uncertainty in the differential pressure drop sensors at these conditions. The oscillation timetable is indicated in figure 6.2.

Although the oscillation has two distinct frequencies, it is a flashing-induced, periodically recurring oscillation and is therefore ranged with the in-phase oscillations in the figures in this chapter.

6.2 Inlet friction distribution

It is expected that some of the stability effects of a power skew can be compensated by adjusting the inlet friction to each channel separately. By increasing

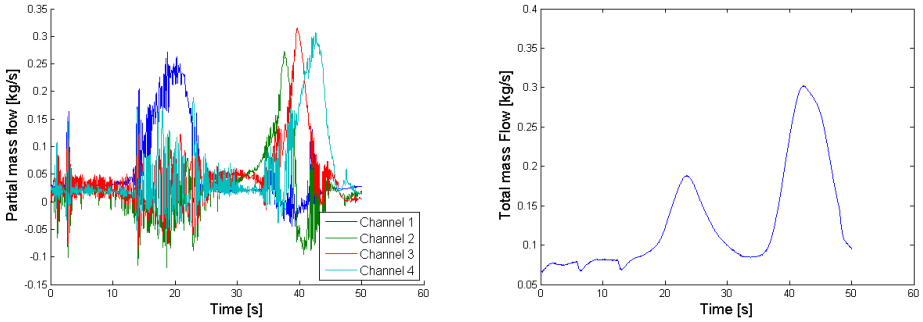

(a) (b)

Figure 6.4: The partial (a) and total (b) mass flow of the instability at $P_{top} = 2,2$ kW (channel 1), $P_{low} = 2,0$kW and $T_{sub} = 17,3$K.

or decreasing the friction component by means of valves, it will be possible to govern the flow through each channel and with that the heat transferred to the coolant per unit of mass. To experimentally test the effect of imposing an inlet friction to a single channel, we will return to the flat power profile and increase the inlet friction coefficient of channel 1 to $K_{in,ch1} = 7,4$. The inlet friction coefficients of the other channels will be kept at their standard values (see table 3.2). The resulting stability map is shown in figure 6.5.

At a first glance, we see the same effects as with the application of a power skew. The system as a whole has become just slightly less stable for a system at a fixed power, while at the same time the in-phase regime is extended downwards in the power-subcooling plane. There are also significant differences however. For example, we see that the out-of-phase and higher order out-of-phase regimes are at the same locations as at equal (low) channel inlet friction, whereas an upward shift was found during power skew experiments. Additionally, when we have a look at the movement of the upper stability boundary in the dimensionless plane in figure 6.6, we see that the increased friction coefficient has a slight stabilizing effect for systems at the same operational point. This result is in accordance with our conclusion about the influence of friction on stability in the previous chapters.

There is another important difference between the power skew and the friction distribution situations. We have seen that in the former case, flashing-induced events occur in each of the four channels, also at power and inlet conditions at which these phenomena would not occur in a flat power profile at P_{low}. This is not the case with the applied friction distribution. Although instabilities for the same system occur at higher subcooling, the instabilities are much less violent. This is due to the fact that at conditions just below the stability boundary only the channel to which the additional friction is applied, shows flashing-induced instabilities, even where these instabilities normally *would* occur in the other channels at equal friction distribution. A schematic representation of the instability is presented in table 6.3. This effect is almost certainly due to higher flows in channels 2, 3 and 4 (after all, at almost the same driving head, partly closing off one channel would force a larger flow in the other channels), but

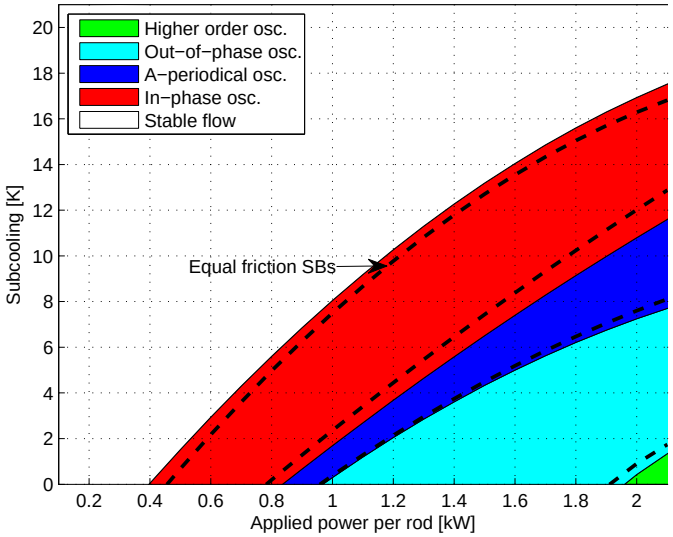

Figure 6.5: The stability map for a situation with a raised inlet friction coefficient in channel 1: $K_{inlet}(ch1) = 7,4$ and $K_{inlet}(ch2-4) \approx 3,4$ (see table 3.2). The dashed lines indicate the stability boundaries in case of equal friction distribution.

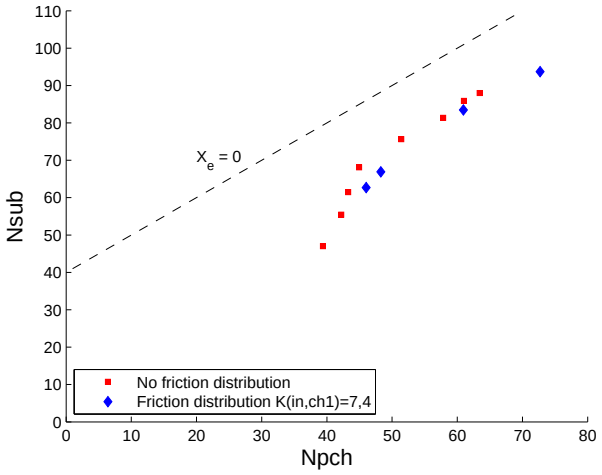

Figure 6.6: The upper stability boundary in case of an enlarged local friction in channel 1 ($K_{in,ch.1} = 7,4$), compared to the case with equal distribution of friction coefficients ($K_{in,ch} \approx 3,4$), see table 3.2.

	t_1	t_2	t_3
Ch.1	F	F	F
Ch.2	↓	↓	↓
Ch.3	↓	↓	↓
Ch.4	↓	↓	↓

Table 6.3: The schematic representation of the instabilities just below the upper stability boundary in case of an inlet friction distribution. The consecutive events are separated by long time intervals.

as before, this could not be experimentally confirmed due to the high relative uncertainty in the differential pressure signal at these conditions.

We can conclude from this that a power skew increases the range of conditions in which flashing-induced instabilities can occur in the low-power channels, while channel inlet friction reduces this range for the low-friction channels. It can therefore be expected that the application of additional local friction to the low-power channels in a skewed power profile, will limit the occurrence of flashing induced instabilities in the high-power channels. At the same time, the occurrence of these instabilities is increased in the channels to which the friction is applied. As a result, the heat transferred to the coolant per unit mass can be equalized over all channels. It would be interesting to investigate if such a combined power and friction skew, would cause the system as a whole to become more stable or less stable.

6.3 Implications for the ESBWR

Returning to the ESBWR itself, we can draw two main implications from the results in the last two sections:

1. One of the most important results is that it was found that a power skew has a destabilizing effect. The thermal hydraulic stability of the system is governed by the channel to which the highest power is applied. This effect has to be taken into account during the startup of the reactor if flashing induced instabilities are to be avoided. In the ESBWR, this effect is expected to be damped by two effects. First of all, the separate channels in the ESBWR are combined into a common riser at a certain height. This means that mixing of the relatively hot coolant and the colder coolant from different channels can be expected, before the coolant reaches the top of the reactor, where the lowest saturation temperature will be encountered. Secondly, due to the large number of channels in the ESBWR, a small number of high-power channels will probably not have a large influence on the mass flow nor on the occurrence of flashing induced phenomena in the other channels. It becomes a completely different situation, however, when there is a cluster of high-power channels. Such a situation could considerably increase the amount of flashing-induced instabilities in the other channels and have a large influence on the mass flow through the system, thus making the whole system less stable.

2. Secondly, we have found that raising the channel inlet friction coefficients slightly destabilizes systems at the same, fixed, power, but has a stabilizing effect for systems at the same operational point. It is expected that incorporating higher local friction coefficients to low-power channels in the design of the reactor can be utilized to even the heat transferred to the coolant per unit mass over the channels.

Chapter 7

Conclusion and Recommendations

7.1 The CIRCUS IV facility

As a result of this project, the CIRCUS IV facility is now fully calibrated and adjusted to allow easier comparison with its predecessors. Many adjustments have been made to the setup: insulation was applied, the thermocouple positions were equalized and the measurement and control of the inlet temperature has been improved significantly. Among the most notable improvements is the installation and implementation of an array of cheap and easy to use optical void sensors. These sensors have shown their value in determining the production of vapor over the complete length of the chimneys at high frequency. In addition to this, the detection of different flow regimes in the facility based on the photodiode signal was shown to be possible. Bubbly flow and in some conditions slug flow, have been seen to produce recognizable signals that were cross-checked with high-speed camera images.

It is believed that the detection of the void regimes can be extended to a point where it is possible to determine the flow regimes throughout the length of the chimney during flashing or geysering events. Besides being very useful to numerical simulation of the time-dependent phenomena in CIRCUS, the information could also provide more understanding of the dynamic processes during flow instabilities and the comparability of different setups. On this topic a bachelor project was formulated and started.

7.2 Instability phenomena

The instability phenomena occurring in a setup with four parallel channels has been investigated in detail. In total, six different stability regimes have been found. Five of these have been shown to be similar to the previously found instability regimes in CIRCUS II. Additionally, the higher order out-of-phase

regime has been identified as a separate regime. The oscillations in this regime often include one or more channels that only show reverse flow. Since the existence of some of the higher order oscillations is clearly linked to the fact that the system has more than two channels, it is expected that more complicated oscillations will arise in systems with even more parallel channels.

It was also found that the behavior in all encountered instability regimes can be explained by a combination of three instability phenomena: flashing, geysering and reverse flow. During in-phase oscillations, all three of these phenomena play a role, whereas out-of-phase oscillations and higher order out-of-phase oscillations are only caused by geysering and reverse flow. In the a-periodical regime, two distinguishable instability mechanisms have been found, a flashing/geysering/reverse flow-induced and a geysering/reverse flow-induced regime. The latter of these a-periodical oscillations only occurs in situations with high reverse flow. The low subcooling stable regime was found to be a combination of continuous flashing in two channels, combined with continuous reverse flow in the other two. Due to the internal circulation in this regime, a hysteresis effect is encountered: more energy needs to be applied to the system to attain this regime than to maintain it. As a result, both a maintenance and an initiation boundary were detected for this regime. It was also found that the low subcooling stable regime could be initiated above the initiation boundary, by applying a perturbation in the form of a power skew or a friction distribution over the channels.

It is expected that detailed study of the higher order out-of-phase regime could result in the determination of another separate regime: the 1 vs 1 vs 1 vs 1 geysering regime. In this case each channel shows a separate geysering instability at equal time intervals. So far, the behavior has been classified with the the higher order regime, but some experiments seem to indicate that there is a fixed region in the power-subcooling plane where 1 vs 1 vs 1 vs 1 oscillations can be observed. Additionally, it is believed to be of interest for many-channel natural circulation systems, to study the pairing of channels during out-of-phase oscillations. At the moment, the process of the two-by-two ordering of geysering channels in this regime is not yet fully understood. If conditions in which out-of-phase oscillations were ever encountered in a reactor, the number of paired channels could have a large influence of the magnitude of the mass flow oscillation.

Finally, it was shown that the in-phase stability boundary for CIRCUS IV is located below the zero quality at the chimney exit line. This means that vapor can be produced during high subcooling stable circulation. This result is in accordance with findings by Manera and Marcel. Furthermore, it was shown by the comparison of the experimentally determined stability boundaries that the unstable operational regime for CIRCUS IV is larger than that of CIRCUS I and II in the dimensionless $N_{pch} - N_{sub}$ plane for high phase change numbers. For lower phasechange numbers, however, CIRCUS IV is more stable. In addition, it was shown that for increasing values of the common inlet friction, the in-phase stability boundary in the dimensionless plane deviates from the zero quality at the chimney exit line, thus increasing the high subcooling stable flow regime. This also means that systems with high common inlet friction are more stable at the same operational point than systems with low common inlet friction.

7.3 Theoretical model and simulation

A simple analytical model was composed to estimate the boundaries of the in-phase and out-of-phase oscillation regimes for natural circulation systems with parallel channels. The model is based on a steady state approximation and the assumption of constant heat loss from the channels. The predictions made by the model, were shown to correspond well to the experimentally determined in-phase and out-of-phase stability boundaries in CIRCUS I, II and IV. Extension of the model to multiple channels, showed that the in-phase and out-of-phase stability boundaries are quite sensitive to channel division. Since they are based on similar assumptions, both boundaries display the same shifts in the power-subcooling and N_{pch}-N_{sub} plane under channel division. It can be concluded from the predictions made by the model, that the overall stability of systems at the same operational point is increased with the amount of chimney division. A system operated at fixed power and inlet temperature conditions, however, experiences a decreased stability at chimney division. For the ESBWR this means that if the same stability characteristics are to be maintained with a divided chimney during startup of the reactor, the power or the inlet temperature has to be reduced.

It is believed that the boundaries of the a-periodical regime and even the higher order out-of-phase and low subcooling stable flow regimes can be predicted based on similar, simple assumptions, when reverse flow is more fully understood and can be modelled for different geometries. The reverse flow is expected to be mainly determined by the values of the local common inlet and chimney exit friction coefficients. A further study into the influence of these frictions on the magnitude of the reverse flow might therefore deliver an approximate relation that can be applied in extending the simple analytical model.

In addition, it is expected that the analytical model can be improved by applying more realistic relations for the heat loss to the surroundings. For the estimation of the stability boundaries, this is not believed to be a significant improvement, but it may shed light on the proportion of the heat loss in the system in comparison to the heat lost in vaporization processes. If the heat loss is relatively large, this could significantly reduce the high subcooling stable regime below the zero quality at the chimney exit line in well insulated reactors and therefore have important consequences for the startup procedure of natural circulation BWRs.

Much effort was also put into the adaptation of a numerical model, created by Marcel [5] for CIRCUS I, to the CIRCUS IV setup. Although this model, in the form it was presented, delivers good results for the single chimney setup, its absence of wall friction terms and the definition of the nodal model, complicate its extension to multiple parallel channels. Furthermore, predictions based on an extension of the model to multiple channels, using similar assumptions as in the simple analytical model used in this thesis, do not correspond with experimental data. It is believed by the author that a broad revision of this model is necessary to be able to apply it to systems of parallel channels as encountered in the ESBWR. It is believed that this model, or a model based on the same method, could be applied to CIRCUS IV successfully in the course of one complete Master's Project or as a part of a PhD research. It would be

especially interesting if the results of such a model were to be combined with the simple analytical model described in Chapter 5. Integrated, they could provide a means to predict most of the boundaries between the stability regimes.

7.4 Power skews

Since the power profile in the ESBWR will not be a flat profile, the effect of the application of a power skew was investigated by applying a higher power to one of the heating rods in CIRCUS IV. It was shown that a power skew destabilizes the system and that the in-phase stability boundary in the power-subcooling plane is governed by the channel to which the highest power is applied. The power skew is shown to not only increase the conditions under which flashing-induced phenomena can occur in the high-power channel, but also in the low-power channels. As a result, the amplitude of the mass flow oscillations is not only governed by the high-power channels.

It was also found that due to a significant power skew, the initiation boundary for low subcooling stable flow is encountered at much higher subcooling. It can be concluded that information about the location of the maintenance boundary for low subcooling stable flow is more useful for ESBWR operation than the determination of the initiation boundary. It might therefore be interesting to investigate the location of the maintenance boundary in the power-subcooling plane and the dimensionless plane in the future.

Furthermore, it was shown that the application of additional local friction to one of the channels, has a stabilizing effect on the system. Also, such a local friction limits the occurrence of flashing-induced instabilities in the remaining, low-friction channels. This finding implies that the differences in the power over mass flow ratio can be equalized over all channels by incorporating channel inlet frictions in the ESBWR. These local frictions should in that case be situated in the low-power channels in the reactor.

It is speculated that a combined power and friction skew has a stabilizing effect on the reactor in the dimensionless N_{pch}-N_{sub} plane as a result of the additional friction added to the system and as a result of equalizing the heat transfer per unit mass over the channels. It may be interesting to research different configurations of power skews and inlet frictions to determine this effect, for example in the course of a Bachelor's project.

Bibliography

[1] Van Bragt, D.D.B. "Analytical Modeling of Boiling Water Reactor Dynamics," (PhD thesis), 1998.

[2] Wissler, E., Isbin, H.S., Amudson, N.R., "Oscillatory Behavior of a Two-phase Natural-circulation Loop," A.I.Ch.E.J. Vol. 2, No. 2, pp. 157-162 (1956).

[3] Van der Hagen., T.H.J.J., Stekelenburg, A.J.C., "The Low-Power Low-Pressure Flow Resonance in a Natural Circulation Boiling Water Reactor," Nucl. Eng. Des., 177,229 (1997).

[4] Manera, A., "Experimental and analytical investigations on flashing-induced instabilities in natural circulation two-phase systems" (PhD thesis), 2003.

[5] Marcel, C.P., "Experimental and Numerical Stability Investigations on Natural Circulation Boiling Water Reactors" (PhD thesis), 2007.

[6] Hinds, D. and Maslak, C. "Next-generation nuclear energy: The ESBWR", Nuclear News, January 2006, pp. 35-40.

[7] "World Energy Outlook 2006," International Energy Agency, 2006.

[8] "Annual energy outlook 2009: Early release overview," International Energy Agency, 2009.

[9] "World Population Prospects," Population division of the United Nations Department of Economic and Social Affairs (2006).

[10] "International Energy Outlook 2008," Energy Information Administration, June 2008.

[11] "Climate change 2007: synthesis report," Intergovernmental Panel on Climate Change, 2007.

[12] "The Carbon Mitigation initiative," Princeton University, www.princeton.edu/~cmi, (2008).

[13] International Atomic Energy Agency: www.iaea.org (2000).

[14] World nuclear association Country briefings: Germany, http://www.world-nuclear.org/info/default.aspx (2008).

[15] "Nuclear Energy Today," Nuclear Energy Agency, 2003. ISBN: 92-64-103228-7.

[16] Hill, P., Bowles, D., Jordan, P., Nathan, R., "Estimating overall risk of Dam Failure: Practical Considerations in Combining Failure Probabilities," ANCOLD risk workshop 2003.

[17] The Association of State Dam Safety officials: http://www.damsafety.org.

[18] "Veiligheid Nederland in kaart, Hoofdrapport onderzoek overstromingsrisico's," november 2005. ISBN: 90-369-5604-8.

[19] Weppelman, G. "Flashing geïnduceerde instabiliteit in de CIRCUS opstelling met vier parallele kanalen" (BsC thesis), 2008.

[20] Janssen, L.P.B.M. and Warmoeskerken, M.M.C.G., "Transport Phenomena Data Companion", Delft University Press, third edition (2001).

[21] Furuya M. Inada, F. and Yasuo, A., "A study on thermalhydraulic Instability of a boiling Natural Circulation Loop with a Chimney (Part II. Experimental Approach to Clarify the Flow Instability in Detail)," Heat Transfer-Jpn. Res., 7, 577 (1995).

[22] Manera, A. and Van der Hagen, T.H.J.J., "Stability of natural-circulation-cooled boiling water reactors during startup: Experimental results." Nuclear Technology, Vol. 143 (2003).

[23] Clausse, A. and Lahey, R.T., "The Analysis of Periodic and Strange Attractors during Density-wave Oscillations in Boiling Flows," Chaos, Solutions and Fractals, Vol 1. No 2. pp. 167-178 (1991).

[24] Haaland, S.E., "Simple and Explicit formulas for the Friction Factor in Turbulent Flow," J. of Fluids Engineering 103 (5), 89-90 (1983).

[25] Oliemans, R.V.A., "Applied Multiphase Flows", Lecture Notes AP3181D, Delft University of Technology, January 2007.

[26] Dekkers, N.H. and Wijnen, J.M.H., "Eenvoudige stromingsleer I", Delta Press, 1989.

[27] Idelchik, I.E. "Handbook of hydraulic resistance." second ed., 1986.

[28] Todreas, N.E. and Kazimi, M.S., "Nuclear Systems I, Thermal Hydraulic Fundamentals," second ed., Taylor & Francis, 1993.

[29] Clause,A., Kerris, A. and Converti, J., "Nonlinear effects on density-wave instabilities in a natural circulating loop," in: Particulate Phenomena and Multiphase Transport, Vol. III (1986), pp. 63-67.

[30] Guido,G., Converti, J. and Clausse, A., "Density-wave oscillations in parallel channels - an analytical approach", in: Nuclear Engineering and Design 125 (1991), pp. 121-136.

Acknowlegdements

I would like to thank Dick de Haas for his patience and enthusiasm in explaining the details of the operation of the CIRCUS IV facility and answering my many questions about the data acquisition and previous setups. In particular, I would like to thank him for personally spot-welding the physical connections for control and data acquisition between the void sensors, power supply and DAQ system.

Also, I would like to thank August Winkelman. He has been helpful in many ways, but especially in coming up with the best method to apply the idea of optical void sensors.

Furthermore, I would like to extend gratitude to Christian Marcel for sending me his model for further study and Annalisa Manera for her helpful attitude and excellent documentation of CIRCUS I data.

Last, but not least, I would like to thank Martin Rohde for his help throughout the project, the thorough feedback on the report and sharing general enthusiasm over new findings. Martin, I'm gonna have to need you to keep up the good work, that would be greeaat. **

Nomenclature

Nomenclature

A	Area $[m^2]$
D	Diameter $[m]$
$\mathbf{F_f}$	Frictional force $[N]$
f	friction coefficient
g	Gravitational acceleration $[\frac{m}{s^2}]$
h	Heat transfer coefficient $[\frac{W}{m^2K}]$
h_l	Liquid enthalpy $[\frac{J}{kg}]$
K	Local Friction factor [-]
K_{in}	Common inlet friction factor [-]
L	Length $[m]$
l	Interval length $[m]$
M	Mass flow $[\frac{kg}{s}]$
N_{pch}	Phase change number [-]
N_{sub}	Subcooling number [-]
P	Power $[W]$
p	pressure $[Pa]$
q	Heat transfer $[W]$
q_{loss}	Heat loss from the channels $[W]$
R	Radius $[m]$
Re	Reynolds number [-]
T	Temperature $[^\circ C]$
t	time $[s]$
$\mathbf{u}$	velocity vector $[\frac{m}{s}]$
v	velocity $[\frac{m}{s}]$

Greek symbols

α	Void fraction [-]
δ	Small perturbation
ε	Relative roughness $[m]$
λ	Heat conductivity $[\frac{W}{mK}]$
ϕ''	Heat flux $[\frac{W}{m^2}]$
χ	Quality [-]
ρ	Density $[\frac{kg}{m^3}]$
τ	Time delay $[s]$

Superscripts and subscripts

avg	Average
c	Core
ch	Channel
ci	Core inlet
dc	Downcomer
fg	Difference between (saturated) vapor and liquid properties
l	liquid
low	Lowest power in power skew
pch	phase change
re	Riser exit = Chimney exit
rf	Reverse flow
sat	saturation
sub	Subcooling
top	Highest power in power skew
up	Upward (flow)
v	vapor

List of Tables

List of Figures

Appendix A

Technical information

Key features of the ESBWR and its predecessors [6].

Parameter	BWR/4	BWR/6	ABWR	ESBWR
Power (MWt/MWe)	3293/1098	3900/1360	3926/1350	4500/1550
Vessel height/dia (m)	21.9/6.4	21.8/6.4	21.1/7.1	27.7/7.1
Fuel bundles, number	764	800	872	1132
Active fuel height (m)	3.7	3.7	3.7	3.0
Power density (kW/L)	50	54.2	51	54
Recirculation pumps	2 (external)	2 (external)	10 (internal)	0
Number/type of CRDs	185/LP	193/LP	205/FM	269/FM
Safety system pumps	9	9	18	0
Safety diesel generators	2	3	3	0
Alternate shutdown	2 SLC pumps	2 SLC pumps	2 SLC pumps	2 SLC accumulators
Control and instrumentation	Analog single channel	Analog single channel	Digital multiple channel	Digital multiple channel
Core damage (freq./yr)	10^{-5}	10^{-6}	2×10^{-7}	3×10^{-8}
Safety bldg vol (m^3/MWe)	120	170	180	130

Appendix B

Thermocouple calibration

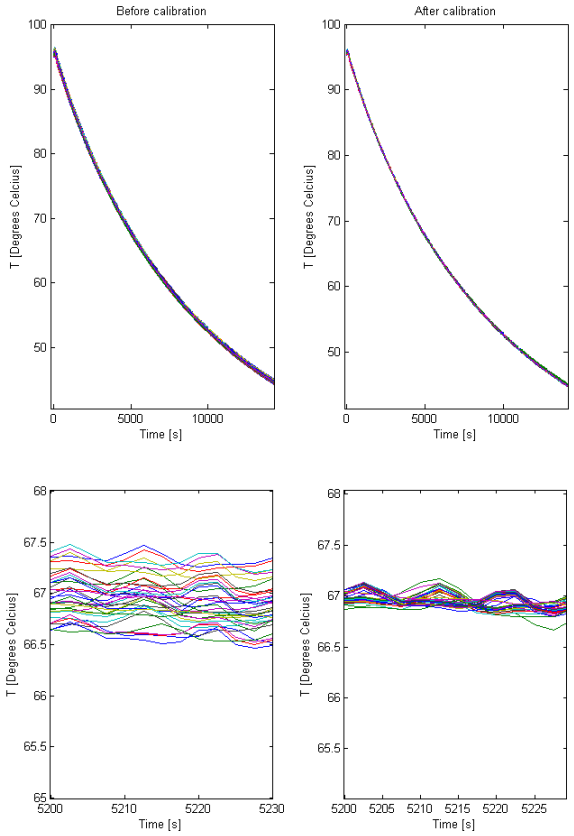

Figure B.1: Thermocouple signals, including the PT100 signals during cooling down of the CIRCUS facility before (left) and after calibration (right). The two images at the bottom are magnifications of the respective upper curves. It can clearly be seen that after calibration the signals are within 0,5 K of each other.

Appendix C

Determination of uncertainty in N_{pch}

The phase change number, N_{pch} is calculated as a function of the power, P and the mass flow M in equation (4.2):

$$N_{pch} = \frac{P}{Mh_{fg}} \frac{\rho_l - \rho_v}{\rho_v} \tag{C.1}$$

The relative uncertainty in N_{pch} can therefore be determined as a function the relative uncertainties in P and M:

$$\left(\frac{u(N_{pch})}{N_{pch}}\right)^2 = \left(1 \cdot \frac{u(P)}{P}\right)^2 + \left(-1 \cdot \frac{u(M)}{M}\right)^2 \tag{C.2}$$

Since it was shown by Weppelman [19] that the relative uncertainty in the determination of the power is very small, we van state that:

$$\left(\frac{u(N_{pch})}{N_{pch}}\right)^2 = \left(-1 \cdot \frac{u(M)}{M}\right)^2 \tag{C.3}$$

Or:

$$u(N_{pch}) = N_{pch} \frac{u(M)}{M}$$

Since the relative uncertainty in the determination of M at low mass flows can become as high as 16%, we see similar relative uncertainties in N_{pch}.

Appendix D

Power skew trends in the dimensionless plane

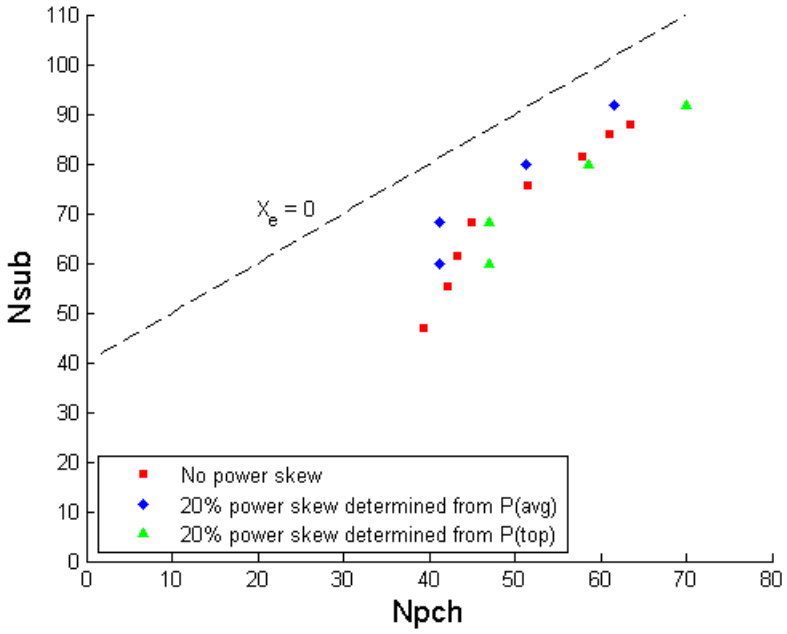

Figure D.1: The upper stability boundary for the flat power profile, compared to the stability boundary of a 20% power skew situation, which is displayed as a function of P_{top} and as a function of P_{avg}.

Appendix E

Equipment specifications

The next pages contain the information sheets of the ultrabright LED and photodiode used in the design of the void sensors.

Ultrabright LED, ∅ 5 mm Untinted Non-Diffused

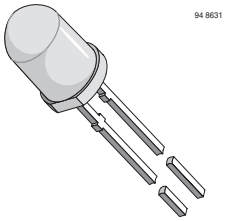

Description

The TLC.58.. series is a clear, non diffused 5 mm LED for high end applications where supreme luminous intensity and a very small emission angle is required.

These lamps with clear untinted plastic case utilize the highly developed ultrabright AlInGaP and GaP technologies.

The very small viewing angle of these devices provide a very high luminous intensity.

Features

- Untinted non diffused lens
- Utilizing ultrabright AlInGaP and InGaN technology
- Very high luminous intensity
- Very small emission angle
- High operating temperature: T_j (chip junction temperature) up to 125 °C for AlInGaP devices
- Luminous intensity and color categorized for each packing unit
- ESD-withstand voltage: 2 kV acc. to MIL STD 883 D, Method 3015.7 for AlInGaP, 1 kV for InGaN

Applications

Interior and exterior lighting

Outdoor LED panels, displays

Instrumentation and front panel indicators

Central high mounted stop lights (CHMSL) for motor vehicles

Replaces incandescent lamps

Traffic signals and signs

Light guide design

Parts Table

Part	Color, Luminous Intensity	Technology
TLCR5800	Red, I_V > 7500 mcd	AlGaP on GaAs
TLCY5800	Yellow, I_V > 5750 mcd	AlGaP on GaAs
TLCTG5800	True green, I_V > 2400 mcd	InGaN on SiC
TLCB5800	Blue, I_V > 750 mcd	InGaN on SiC

Absolute Maximum Ratings

T_{amb} = 25 °C, unless otherwise specified
TLCR5800 , TLCY5800 , TLCTG5800 , TLCB5800

Parameter	Test condition	Part	Symbol	Value	Unit
Reverse voltage			V_R	5	V
DC forward current	T_{amb} ≤ 85°C	TLCR5800	I_F	50	mA
	T_{amb} ≤ 85°C	TLCR5800	I_F	50	mA
	T_{amb} ≤ 60°C	TLCTG5800	I_F	30	mA
	T_{amb} ≤ 60°C	TLCTG5800	I_F	30	mA

TSL250R, TSL251R, TSL252R
LIGHT-TO-VOLTAGE OPTICAL SENSORS

TAOS028F − NOVEMBER 2005

- **Monolithic Silicon IC Containing Photodiode, Operational Amplifier, and Feedback Components**
- **Converts Light Intensity to a Voltage**
- **High Irradiance Responsivity, Typically 137 mV/(μW/cm²) at λ_p = 635 nm (TSL250R)**
- **Compact 3-Lead Clear Plastic Package**
- **Single Voltage Supply Operation**
- **Low Dark (Offset) Voltage....10 mV Max**
- **Low Supply Current.....1.1 mA Typical**
- **Wide Supply-Voltage Range.... 2.7 V to 5.5 V**
- **Replacements for TSL250, TSL251, and TSL252**
- **RoHS Compliant (−LF Package Only)**

PACKAGE S
SIDELOOKER
(FRONT VIEW)

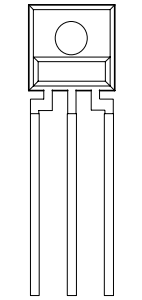

PACKAGE SM
SURFACE MOUNT
SIDELOOKER
(FRONT VIEW)

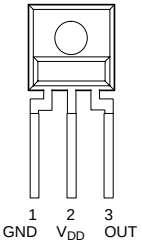

Description

The TSL250R, TSL251R, and TSL252R are light-to-voltage optical sensors, each combining a photodiode and a transimpedance amplifier (feedback resistor = 16 MΩ, 8 MΩ, and 2.8 MΩ respectively) on a single monolithic IC. Output voltage is directly proportional to the light intensity (irradiance) on the photodiode. These devices have improved amplifier offset-voltage stability and low power consumption and are supplied in a 3-lead clear plastic sidelooker package with an integral lens. When supplied in the lead (Pb) free package, the device is RoHS compliant.

Functional Block Diagram

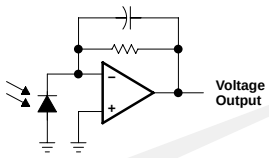

Available Options

DEVICE	T_A	PACKAGE − LEADS	PACKAGE DESIGNATOR	ORDERING NUMBER
TSL250R	0°C to 70°C	3-lead Sidelooker	S	TSL250R
TSL250R	0°C to 70°C	3-lead Sidelooker — Lead (Pb) Free	S	TSL250R−LF
TSL250R	0°C to 70°C	3-lead Surface-Mount Sidelooker — Lead (Pb) Free	SM	TSL250RSM−LF
TSL251R	0°C to 70°C	3-lead Sidelooker	S	TSL251R
TSL251R	0°C to 70°C	3-lead Sidelooker — Lead (Pb) Free	S	TSL251R−LF
TSL251R	0°C to 70°C	3-lead Surface-Mount Sidelooker — Lead (Pb) Free	SM	TSL251RSM−LF
TSL252R	0°C to 70°C	3-lead Sidelooker	S	TSL252R
TSL252R	0°C to 70°C	3-lead Sidelooker — Lead (Pb) Free	S	TSL252R−LF
TSL252R	0°C to 70°C	3-lead Surface-Mount Sidelooker — Lead (Pb) Free	SM	TSL252RSM−LF

Texas Advanced Optoelectronic Solutions Inc.
1001 Klein Road • Suite 300 • Plano, TX 75074 • (972) 673-0759
www.taosinc.com